NTNU
Norwegian University of
Science and Technology

Master's thesis

# Construction of a Transport Kernel for an Ensemble Monte Carlo Simulator

Øyvind Olsen

**Abstract**

Carrier-carrier interactions and the implementation of the Pauli principle are the main focus of this report. These effects provided satisfactory results such as an improved cooling mechanism for electrons having been exposed to an external field. Additional work was invested in simulating the material $Cd_xHg_{1-x}Te$ in addition to the more common GaAs. This work included alloy scattering mechanisms and implementation of a new, empirical, band structure. This implementation involves careful determination of the final momentum vector in order to conserve energy in the simulations. The calculation of scattering rates was pre-tabulated which greatly reduced simulation times. Several key concepts in Ensemble Monte Carlo simulations were investigated, such as self-scattering and superparticles, in order to provide a consistent theoretical background and illuminate needed corrections. Results are reviewed mainly through considering the average energy of the system and the momentum-space distribution of carriers since physical intuition applies well to these quantities.

June 15th 2009

NTNU
Norwegian University of
Science and Technology

Masteroppgave

# Konstruksjon av en Transportkjerne for en Ensemble Monte Carlo-Simulator

Øyvind Olsen

**Sammendrag**

Implementasjonen av ladningsbærerinteraksjon og Pauli-prinsippet i halvledere er hovedfokuset i denne rapporten. Disse effektene resulterte i en forbedret avkjølingsmekanisme for elektronene etter påsatt felt. Arbeidet har også gått til å simulere $Cd_xHg_{1-x}Te$ i tillegg til det tradisjonelle GaAs. Dette involverte implementering av en ny båndstruktur og spredinger på grunn av legeringer. I tillegg kommer en nøyaktig bestemmelse av den endelige impulsvektoren etter spredinger som sørger for å bevare energien i simuleringene. Spredingsratene blir nå også tabulert på forhånd slik at programmet er raskere. Sentrale deler av Monte Carlo algoritmen, som superpartikler og "self-scattering", undersøkes for å belyse mangler i programmet samt å underbygge resultater. Resultatene vurderes hovedsakelig via gjennomsittsenergien og ladningsbærernes fordeling i det resiproke rom.

15. Juni 2009

# Preface

This master's thesis constitutes the 10th semester of the master degree study in technical physics at the Department of Physics at the Norwegian University of Science and Technology (NTNU), and is a continuation of my project assignment "Modeling of Hole Scattering in a Monte Carlo Transport Kernel for Semiconductors" [1] carried out in the autumn of 2008.

I would like to thank all those who helped out along the way, and also to those that helped read through this report towards the end. Especial thanks goes to Trond Brudevoll and Ole Christian Norum whose help and support was much appreciated. Also thanks to Asta-Katrine Storebø and Jon Andreas Søvneng for their involvement in the project. The program code can be obtained by sending an email to the author at olsen__@hotmail.com.

# Contents

# Chapter 1

# Introduction

$Cd_xHg_{1-x}Te$, or cadmium mercury telluride (CMT), is one of the most promising semiconductors for modern technology. It is an alloy of CdTe and HgTe, of which the former has a bandgap of 1.5 eV at room temperature, while HgTe is a semi metal, i.e. it has no bandgap. Forming an alloy from these two components can yield a semiconductor with any bandgap between 0 and 1.5 eV, depending on the ratio. Because of this CMT can be manufactured to have its optical absorption at a desired infrared wavelength. Naturally this results in many promising applications such as thermal imaging, night vision and imaging through dense fog. Such possible applications is the reason CMT is undergoing extensive study at Norwegian Defence Research Establishment (FFI).
In this context simulations of laser pulse on semiconductor materials could greatly assist in understanding experimental results. This report deals with the work in progress concerning the development of such a simulation tool. In particular, the Monte Carlo method is well suited to the task, and a kernel for such a program has already been developed. In this report the latest improvements to the kernel are described.
Such programs have, of course, been developed in the past, but the need has resurfaced in recent years, especially as device dimensions continue to decrease. A modern program, like we are creating, will have many benefits over its pre-millennium counterparts. Many advancements in the theoretical understanding of semiconductor phenomenons have been made, and these can now be implemented. In addition, programming languages and techniques are rapidly evolving and this enables more efficient and comprehensible coding.

Recent developments in the understanding of phenomenons such as carrier-carrier, carrier-plasmon, carrier-coupled longitudal optical phonon and plasmon modes as well as hot phonons underscores the relevance and importance of the MC program we are developing. Particle movements in THz devices and quantum corrections for small scale ($\sim$ 10nm) electronic devices requires a revision of any pre-millennium programs.

Simulation of hot phonon effects was necessary in the mid- and late 1990's to understand and explain the slow cooling rate of the carrier plasma observed in pump-probe laser experiments. Such simulations requires evaluation of electron and hole dynamics as well as the phonon temperature,which, in the hot phonon case, is different for the optical and acoustic modes. The evaluation of energy transfer problems is therefore a key element in a modern Monte Carlo program. In recent times different alloys are of technological

importance. GaAs- and CMT-alloys require a flexible and realistic representation of of the band structure which may change significantly by varying the alloy fraction and lattice temperature. This aspect is more important today than $\sim 20$ years ago.

In this report carrier-carrier interactions are investigated. These interactions are expected to play an important role in the cooling of the electron gas. These interactions are of increasing importance as the density of carriers rise. In such cases the quantum mechanical exclusion effect, known as the Pauli exclusion principle, will also play an important role, especially in narrow-gap semiconductors[2], and is therefore also considered in this report. The material simulated previously has been GaAs due to the abundance of data available. In this work $Cd_xHg_{1-x}Te$ is added as a simulated material, and the work includes changes to the band structure as well as the introduction of alloy scatterings. The introduction of CMT is eased since it and GaAs both have Zincblende structure, though two distinct versions of the program were kept, one for each material. Note also that, in addition to what is described in this report, others have worked on the implementation of a Poisson solver and hot phonons[3]. This is mentioned to show that care is taken to ensure that the finished program will include most of the effects considered important for current simulations. The work done on the Monte Carlo program will be included in FFI's contribution to the Edison conference[4] later this year.

With the construction of a program like the one described here, many technical improvements (and mistakes) are made along the way, most of which are not worthy of mention in this report. Most minor issues have therefore been omitted due to their rather tedious and unimportant nature.

In chapter 2 the underlying theory of the various considered effects is reviewed. Also the methods of implementation into the program are given since they are described in a theoretical way. The results of the simulations are shown and discussed in chapter 3, naturally with specific emphasis on the recent changes. Finally, in chapter 4, some conclusions are drawn and areas of further work are considered. Last are some appendices concerning more in-depth calculations.

# Chapter 2

# Theory and implementation

In this chapter the new additions to the Monte Carlo program are described. A brief review of the relevant theory is given where appropriate and the methods of implementation into the program are described. Note that only the work on significant changes are described and details technical difficulties are omitted.

## 2.1 Scattering theory

This section describes the theory behind the newly implemented scattering rates, as well as briefly reviewing some parts of the general theory where necessary.

### 2.1.1 Bloch's theorem

When considering a periodic crystal structure, the background potential has the same periodicity as the crystal lattice, $R$. Therefore a property of the background potential seen by the electrons is[5]

$$U(\mathbf{r}+\mathbf{R}) = U(\mathbf{r}) \tag{2.1}$$

Since each cell in the crystal is identical the electron probability must also the same in each such cell. One obtains

$$|\psi(\mathbf{r}+\mathbf{R})|^2 = |\psi(\mathbf{r})|^2 \tag{2.2}$$

Bloch's theorem states that such an electron state is made up of a plane wave and a function, $u_{\mathbf{k}}(\mathbf{r})$, with the same periodicity as the crystal, i.e.

$$\psi_{\mathbf{k}}(\mathbf{r}) = e^{i\mathbf{kr}} u_{\mathbf{k}}(\mathbf{r}) \tag{2.3}$$

where $u_{\mathbf{k}}(\mathbf{r}) = u_{\mathbf{k}}(\mathbf{r}+\mathbf{R})$. The eigenstate of the electron thus has the following property

$$\psi_{\mathbf{k}}(\mathbf{r}+\mathbf{R}) = e^{i\mathbf{kR}} \psi_{\mathbf{k}}(\mathbf{r}) \tag{2.4}$$

These eigenstates form the basis for calculating the scattering rates in the Monte Carlo program.

### 2.1.2 Scattering probabilities

In the current work all scattering probabilities are based on Fermi's Golden Rule (FGR) given as[5]

$$\Gamma(k,k') = \frac{2\pi}{\hbar}\left|\langle i|H'_{k,k'}|f\rangle\right|^2 \delta(\epsilon_f - \epsilon_i) \tag{2.5}$$

where $H'$ is the interaction potential and $\epsilon_i$ and $\epsilon_f$ are the energies before and after the scattering. For further details on the scattering of individual processes see the project work[1]. In order to determine the final state, or more specifically the scattering angles, various techniques are used. These involve employing random numbers to test scattering angles against the angular probability distribution. For details see the project work[1].

### 2.1.3 Alloy scattering

Due to the inherent disorder present in alloys, electrons and holes scatter as they propagate through the material. Because of this a simple model for alloy scattering was implemented in the Monte Carlo program. In the following a perfectly random alloy is assumed where the smallest physical size over which the crystal potential can fluctuate is the unit cell. The alloy potential given as $U_{all}$ is not well defined and must be adjusted to experimental data. The total scattering rate for such a process is[5]

$$\Gamma_{alloy} = \frac{3\pi^3}{8\hbar} V_0 U_{all}^2 x(1-x)N(E) \tag{2.6}$$

where $x$ is the alloy fraction, $V_0$ is the volume of the unit cell and $N(E)$ is the density of states. In the implementation a simple model for the density of states was used[5]

$$N(E) = \frac{m^*\sqrt{m^*E}}{\sqrt{2}\pi^2\hbar^3} \tag{2.7}$$

### 2.1.4 Acoustic rates

The acoustic scattering rates were updated to account for a non-parabolic bandstructure. This was implemented directly as described by Brudevoll *et.al.*[6] and all details are given in the reference. This did not alter the scattering rates significantly, therefore the alteration is only briefly mentioned.

## 2.2 The Ensemble Monte Carlo method

In this section the Ensemble Monte Carlo method (EMC) and some of the more important implemented concepts will be described. The abbreviation Monte Carlo(MC) is sometimes used, though they are not strictly the same. The latter refers to iterated simulations of a single carrier while in the EMC-method each iteration simulate many carries simultaneously. In the current work we have used the EMC-method at all times and this is what is meant by 'Monte Carlo' on all occasions. The advantage, indeed the necessity, of using the EMC-method emerges when simulating interacting particles. Such

interactions are shown in the section 2.3 and 2.4 dealing with carrier-carrier interaction and the Pauli-principle.

### 2.2.1 Program description

A flowchart of the program is given in figure 2.1. The Monte Carlo program includes options for an external field, number of simulation steps and carriers, initial distribution of the electrons and whether to include carrier-carrier interactions, a Poisson solver, hot phonons and/or the Pauli principle. More details on the workings of the program can be found in Norums thesis[3]. Whether or not it is time for an individual particle to scatter or not is described in the next section.

### 2.2.2 Free flight and Self-scattering

The expression 'free flight-time' refers to the time spent by a particle moving, perhaps under the influence of an external field, between scattering events. Note that this procedure was not accurately implemented and had to be rectified by the author. If the probability that a carrier will scatter during the time d$t$ is $p(t)$d$t$, and if it scattered at $t = 0$, then the probability that it has not scattered again is[7]

$$\exp\left[-\int_0^t p(t')\mathrm{d}t'\right] \tag{2.8}$$

The probability $p(t)$ must,in general, be time-dependent since it is dependent on the energy which can change during free flight due to an external field. The probability of a particle scattering in the interval $dt$ around t is then given by[7]

$$P(t) = p(t)\exp\left[-\int_0^t p(t')\mathrm{d}t'\right] \tag{2.9}$$

This cumbersome expression is to numerically costly to solve. Fortunately the 'self-scattering' approach can be applied[7]. If $\Gamma$ is the maximum value of $p(t)$ in the energy-region of interest, then an additional 'self-scatter' term is introduced so that

$$p(t) + \Gamma_{self-scatter} = p(t)_{max} = p_{max} = \Gamma \tag{2.10}$$

using this, time-independent, probability eq. (2.9) simplifies to

$$P(t) = \Gamma\exp\left[-\Gamma t\right] \tag{2.11}$$

and applying the direct technique[7] [1] an expression for the flight-time is obtained

$$r = \int_0^{t_r} \Gamma\exp\left[-\Gamma t'\right]\mathrm{d}t' \;=>\; t_r = -\frac{\ln(r)}{\Gamma} \tag{2.12}$$

where $r \in [0, 1]$. An alternative, and complete, derivation by the author is presented in appendix B. When selecting the occurred scattering mechanism for a single carrier, any choice so that

$$r\Gamma > \int_0^{t_f} P(t)\mathrm{d}t = \sum_i^M \Gamma_i(E(t)) \tag{2.13}$$

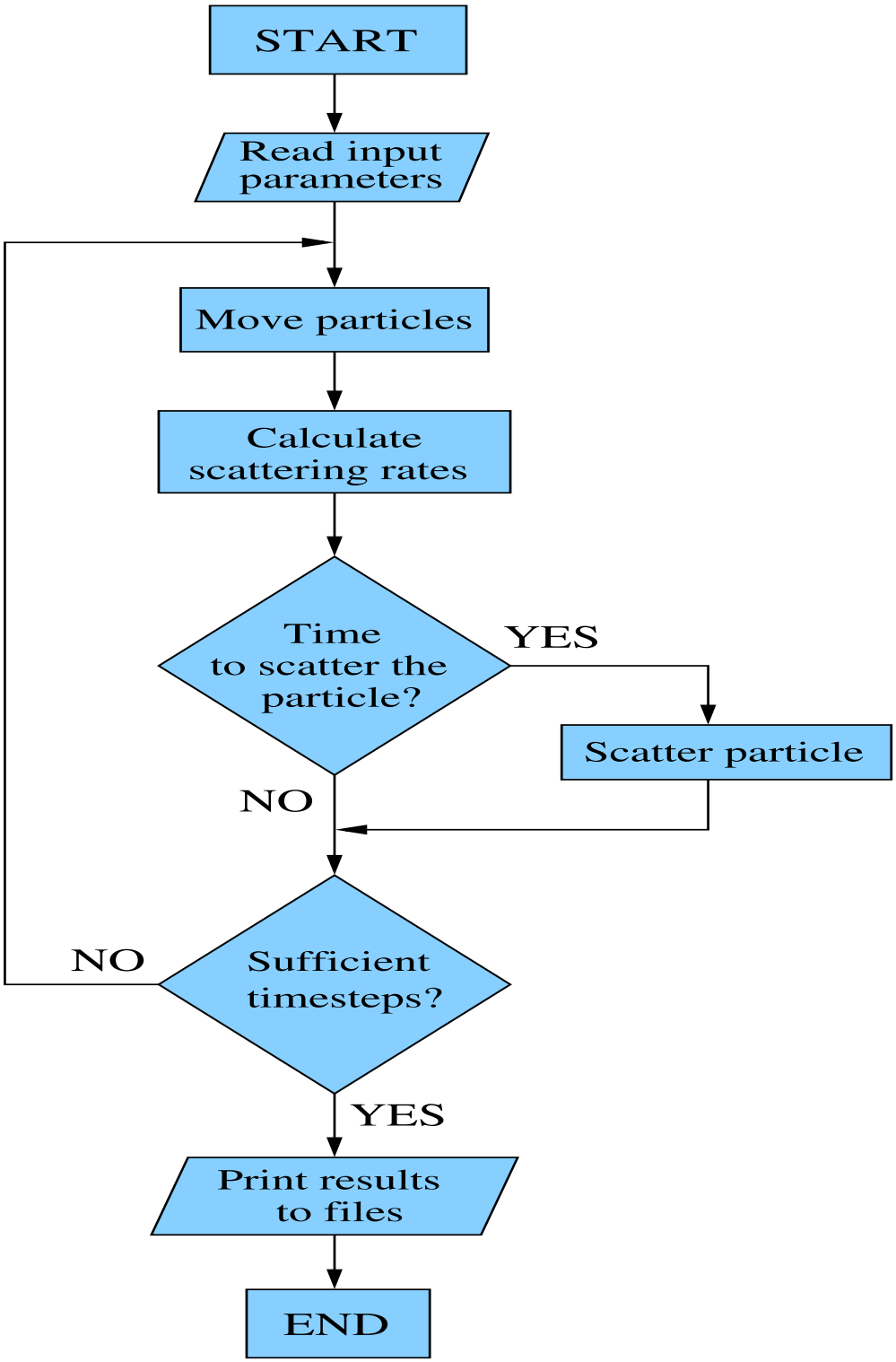


**Figure 2.1:** Flowchart of the Monte Carlo program. The particles are moved and scattered a number of times equal to some predetermined number.

results in a 'self-scattering' where the particle continues unscathed without any changes to its momentum. Here $\Gamma_i(E(t))$ are the various scattering processes possible for the carrier with the current,time dependent, energy. When the inequality in eq. (2.13) is not fulfilled the scattering mechanism $j$ is selected so that

$$\sum_{i=1}^{j-1} \Gamma_i(E(t)) < r\Gamma < \sum_{i=j}^{M} \Gamma_i(E(t)) \tag{2.14}$$

where $M$ is the total number of available scattering processes. Self-scatterings are of course wasted computer time, but it is still cheaper than solving eq. (2.9) directly. This method requires the maximum, total scattering rate for each valley and band. This is obtained through a pre-tabulation of the scattering rates as described in the next section.

### 2.2.3 Tabulated rates

Tabulated rates were implemented into the program by using look-up tables for the scattering rates and carrier energy. When comparing the energy of the carrier to the discrete energy table, a choice must be made since this energy usually lies between two tabulated ones, i.e.

$$E_i < E < E_{i+1} \tag{2.15}$$

Either of the energies could be chosen with relatively small errors in the scattering rates, but better approach is to interpolate the contributions from both relevant scattering rates so that

$$\Gamma(E) = (1-x)\Gamma_i + x\Gamma_{i+1} \tag{2.16}$$

where $x = \frac{E-E_i}{E_{i+1}-E_i}$, i.e. the relative distance from $E_i$ to $E_{i+1}$. This reduces energy conservation problems in the Monte Carlo program. Examples of such problems are the processes involving emission of a boson. Conservation rules require that $E > \hbar\omega$. So if $E_{i+1}$ is chosen in eq. (2.15), and if the situation is such that

$$E_i < E < \hbar\omega < E_{i+1}$$

a non-zero rate would be given for the mechanism and it ends up with $E_f < 0$. This is clearly unphysical and must be avoided. The procedure in eq. (2.16) lessens this problem by scaling the rates according to the energies and improves the accuracy of the tabulated rates.

### 2.2.4 Superparticles

In a simulation of any meaningful size one cannot simulate every single electron. In stead the concept of superelectrons, or superparticles in general, is introduced. This means setting the number of simulated particles to a fixed number at the start of the simulation so that each such superparticle represents a number of actual particles depending on their density. The superparticle is considered as behaving as the average electron or hole in a group of that size would. It is a basic assumption of the Ensemble Monte Carlo method that this represents the behavior of electrons with sufficient accuracy

even though this will depend on the number of superparticles. Special care must be taken when considering interacting particles and precise handling is necessary. An useful concept is the ratio between the number of real carriers and superparticles. If these are $N_e$ and $N_{sup}$, respectively, and $n$ denotes density, then

$$N_{ratio} = \frac{N_e}{N_{sup}} = \frac{n_e}{n_{sup}} = \frac{n_e V}{N_{sup}} \tag{2.17}$$

gives the number of real electrons represented by each superelectron. It should be noted that in current simulations a 2D Poisson solver is included while the program otherwise operates in a three dimensional k-space. The interpretation of $N_{sup}$ in this situation is fully described by Jensen[8]. In short, the superparticles can be said to represent the density in the dimension that is not accounted for. The relation between real carriers and superparticles is important when the carrier-carrier scattering and the Pauli principle is introduced below.

## 2.3 Carrier-carrier scattering

Carrier-carrier scattering mechanisms were implemented in the Monte Carlo program. This was done following the procedures of Mosko[9],Ferry[10] and Jacoboni and Lugli[7] and the theory will be briefly reviewed here.

### 2.3.1 Carrier-carrier interaction theory

The interaction between carriers can be analyzed using the Hamiltonian

$$H_e = \sum_i \frac{p_i^2}{2m} + \frac{e^2}{2\kappa} \sum_{i,j,j\neq i} \frac{1}{|r_i - r_j|} \tag{2.18}$$

where $\kappa = 4\pi\epsilon$. The terms are the free carrier energy and the Coulomb interaction, respectively. Using the random phase approximation (RPA), this can be written as a sum of four different terms[11]. These terms can be written in terms of creation and annihilation operators in the following way.

$$\begin{aligned}
H_e^k &= \sum_k \frac{\hbar^2 k^2}{2m} c_k^\dagger c_k \\
H_e^{Sc} &= \sum_{k>q_c} \frac{2\pi e^2}{V\kappa k^2} \sum_{\lambda,\mu} c_{k_\lambda+k}^\dagger c_{k_\mu-k}^\dagger c_{k_\mu} c_{k_\lambda} \\
H_e^{pl} &= \sum_k \hbar\omega_p (a_k^\dagger a_k + \frac{1}{2}) \\
H_e^{e-pl} &= \sum_{k<q_c} \left( \frac{\pi e^2 \hbar^2}{2V\kappa\omega_p m^2 k^2} \right)^{1/2} \times \sum_{k'} (2k\cdot k' + k^2)(a_{k'}^\dagger c_{k-k'}^\dagger c_k + a_{-k} c_{k'-k}^\dagger c_{k'})
\end{aligned} \tag{2.19}$$

where $a_k^\dagger$,$a_k$ are creation-and annihilation operators for the bosons, and $c_k^\dagger$,$c_k$ for the electrons. The first term, $H_e^k$, describes the free electron kinetic term. The second term,

$H_e^{Sc}$, describes the electron-electron interaction and $H_e^{pl}$ describes the energy of the boson gas, or plasmons. The last term, $H_e^{e-pl}$, describes the electron-plasmon interaction or the long range carrier interaction. To separate the short-and long range parts of the carrier interaction $q_c$ has been introduced. This can be approximated with the Debye screening length[7]

$$q_c \approx \beta \approx \left(\frac{n_e e^2}{\epsilon k_B T_e}\right)^{1/2} \tag{2.20}$$

Here $T_e$ is the electron temperature. If holes are present in the simulation, the equivalent term for holes is added. The second and fourth term in eq. (2.19) give the dynamics of the system and will therefore be the main focus.

### Short-range interaction

Using the second term in eq. (2.19) and the Fermi Golden rule, we can show that the scattering rate for the short range interaction is

$$S_{k_0,k\to k_0',k'} = \frac{2\pi}{\hbar}|M|^2 f_{k_0} f_k (1-f_{k_0'})(1-f_{k'})\delta(\epsilon_{k_0'} + \epsilon_{k'} - \epsilon_{k_0} - \epsilon_{k_0}) \tag{2.21}$$

where $f$'s are the occupation probabilities. If parabolic bands and screened potential are assumed and we use the plane wave approximation the matrix element becomes

$$M = \left\langle k_0, k \left| \frac{e^2}{\kappa r} e^{\beta r} \right| k_0', k' \right\rangle = \frac{4\pi e^2}{V\kappa} \frac{\delta_{k_0+k,k_0'+k'}}{|k'-k_0|^2+\beta^2} \tag{2.22}$$

where $V$ is some arbitrary integration volume. The resulting scattering rate becomes

$$\Gamma_{e-e}(k_0) = \frac{me^4}{\hbar^3 V\kappa^2} \sum_k f_k \frac{|k-k_0|}{\beta^2\left(|k-k_0|^2+\beta^2\right)} \tag{2.23}$$

This expression is unpractical because it demands specific knowledge of the distribution function. However, as shown by Ferry and Osman[10], this can be made more suitable for Ensemble Monte Carlo simulations due to the built-in nature of the distribution function. Replacing the sum in eq.(2.23) with an integral and realizing that

$$\langle G \rangle = \int d^3k\, f(k) G(k) = \frac{1}{N}\sum_i^N G_i(k) \tag{2.24}$$

where $N$ is the number of carriers,$G_i(k)$ is some microscopic observable and $\langle G \rangle$ is the ensemble average. Using this the scattering rates are[10]

$$\begin{aligned}
\Gamma_{eh}(k_0) &= \frac{p\mu e^4}{2\pi\epsilon^2\hbar^3}\frac{1}{N_h}\sum_{holes}\frac{Q_{eh}}{\beta^2\left(Q_{eh}^2+\beta^2\right)} \\
\Gamma_{he}(k_0) &= \frac{n\mu e^4}{2\pi\epsilon^2\hbar^3}\frac{1}{N_e}\sum_{electrons}\frac{Q_{he}}{\beta^2\left(Q_{he}^2+\beta^2\right)} \\
\Gamma_{ee}(k_0) &= \frac{nme^4}{4\pi\epsilon^2\hbar^3}\frac{1}{N_e}\sum_k\frac{|k_0-k|}{\beta^2\left(|k_0-k|^2+\beta^2\right)}
\end{aligned} \tag{2.25}$$

where $n$ and $p$ are the electron and hole density, $\mu$ is the reduced mass of the carriers. Also

$$Q_{eh} = 2\mu \left| \frac{k_0}{m_e} - \frac{k}{m_h} \right| \tag{2.26}$$

The hole-hole scattering is equivalent to the last term in eq.(2.25). It should be noted that the rates used here assume a parabolic bandstructure like most other rates in the program.

### Long range interaction (plasmons)

The long range part of the carrier-carrier interaction is sometimes called the carrier-plasmon interaction. This is because, as seen from the fourth term in eq. (2.19), the plasmons are the quantized excitations of the electron gas just as phonons are for the ions. Therefore it was handled much like impurity and phonon scattering, since it only depends on the energy and only affects one carrier. Details of such scatterings can be found in the project[1]. In the case of plane waves the matrix element is[7]

$$|M|^2 = \frac{\pi e^2 \hbar^3}{2V\kappa\omega_p q^2 m^2}(2\mathbf{k}\cdot\mathbf{q}+q^2)^2[N_q\delta(\epsilon_{k+q}-\epsilon_k-\hbar\omega_p)+(N_q+1)\delta(\epsilon_{k-q}-\epsilon_k+\hbar\omega_p)] \tag{2.27}$$

where $N_q$ is the Bose-Einstein equilibrium distribution population for the plasmons and $\mathbf{q}$ is the wavevector for the plasmon involved. The plasma frequency is, assuming heavy ions, given by[12]

$$\omega_p = \left( \frac{4\pi e^2 n_e}{m^* \epsilon_\infty} \right)^{1/2} \tag{2.28}$$

The electron emits or absorbs a plasmon similar to the phonon interactions. $q_c$ will in this case be the upper limit that defines the maximum wavevector for which a plasmon exists as an independent excitation of the electron gas. It is given as either the inverse Debye screening length in eq. (2.20) or the maximum value of the phonon wavevector whichever is smaller, as shown by Singh[5].

$$q_{phonon\,max} = 2k\left[1 \pm \frac{v_s m*}{\hbar k}\right] \tag{2.29}$$

Here $v_s$ is the sound velocity and $k$ is the electron wavevector. In the following $k_p$ is associated with the plasmon frequency so that $E(k_p) = \hbar\omega_p$ The scattering rate is given in the following form for emission[7] when $k > k_p$

$$\begin{aligned}
\Gamma^{e-pl}(k) = & \\
& k_p > q_c \\
& = \begin{cases} C(N_q+1)\ln\frac{q_c/k}{1-(1-\hbar\omega_p/\epsilon_k)^{1/2}}, & k > \frac{q_c^2+k_p^2}{2q_c} \\ 0, & k_p < k < \frac{q_c^2+k_p^2}{2q_c} \end{cases} \\
& k_p < q_c \\
& = \begin{cases} C(N_q+1)\ln\frac{1+(1-\hbar\omega_p/\epsilon_k)^{1/2}}{1-(1-\hbar\omega_p/\epsilon_k)^{1/2}}, & k_p < k < \frac{q_c^2+k_p^2}{2q_c} \\ C(N_q+1)\ln\frac{q_c/k}{1-(1-\hbar\omega_p/\epsilon_k)^{1/2}}, & k > \frac{q_c^2+k_p^2}{2q_c} \end{cases}
\end{aligned} \tag{2.30}$$

and for absorption the scattering rate is

$$\Gamma^{e-pl}(k) = \begin{array}{l} k_p > q_c \\ = \begin{cases} CN_q \ln\frac{q_c/k}{-1+(1+\hbar\omega_p/\epsilon_k)^{1/2}}, & k > \frac{-q_c^2+k_p^2}{2q_c} \\ 0, & k < \frac{-q_c^2+k_p^2}{2q_c} \end{cases} \\ k_p < q_c \\ = \begin{cases} CN_q \ln\frac{1+(1+\hbar\omega_p/\epsilon_k)^{1/2}}{-1+(1+\hbar\omega_p/\epsilon_k)^{1/2}}, & k > \frac{q_c^2-k_p^2}{2q_c} \\ CN_q \ln\frac{q_c/k}{-1+(1+\hbar\omega_p/\epsilon_k)^{1/2}}, & k < \frac{q_c^2-k_p^2}{2q_c} \end{cases} \end{array} \tag{2.31}$$

where

$$C = \frac{me^2\omega_p}{\kappa\hbar^2 k}$$

The above expressions are rather cumbersome, but are well suited for numerical purposes and are therefore given in the current form. The final state is chosen using the same technique as for polar optical phonon scattering according to the angular probability distribution [7]

$$P(\beta)d\beta = \frac{\sin\beta d\beta}{\epsilon + \epsilon' - 2\sqrt{\epsilon\epsilon'}\cos\theta} \tag{2.32}$$

where $\epsilon$ and $\epsilon'$ are the energies before and after the scattering.

### 2.3.2 Implementation of carrier-carrier scattering

The short range part of the carrier-carrier scattering must be handled differently than other scattering mechanisms in the program. This is because it involves two carriers and also because it is dependent on the wavevector **k**, and not just the energy. The mechanism is therefore implemented as a stand-alone subroutine in the Monte Carlo program that is executed every simulation step. Part of the procedure described here is similar to the 'self-scattering' approach described above. Below, only electron-electron interactions are considered since the hole-hole and electron-hole mechanisms were implemented in the same way. The probability of interaction between two specific electrons can be described by removing the sum over partner electrons in eq. (2.25)

$$\Gamma_{e-e}(k_0, k) = \frac{nme^4}{4\pi\epsilon^2\hbar^3}\frac{1}{N_e}\frac{|k_0 - k|}{\beta^2\left(|k_0 - k|^2 + \beta^2\right)} \tag{2.33}$$

where $N_e$ is the number of real electrons. The program uses superparticles, however, and the above rate cannot be implemented without some additional consideration regarding the relation between superparticles and real electrons. From eq. (2.17) the number of represented electrons is obtained as $N_{ratio}$. Multiplying with this factor permits the rate

to be used on superparticles.

$$\begin{aligned}\Gamma_{e-e,sup}(k_0,k) &= N_{ratio}\Gamma_{e-e}(k_0,k) = \frac{N_e}{N_{sup}}\Gamma_{e-e}(k_0,k)\\ \Gamma_{e-e,sup}(k_0,k) &= \frac{nme^4}{4\pi\epsilon^2\hbar^3}\frac{1}{N_{sup}}\frac{|k_0-k|}{\beta^2\left(|k_0-k|^2+\beta^2\right)}\end{aligned} \tag{2.34}$$

This shows that using number of superparticles, $N_{sup}$, when calculating the rates in the program is correct. It must be emphasized that the rate in eq. (2.34) is between two specific superparticles. To obtain the rate equivalent to Ferry's rate in eq. (2.25), one should sum over all possible scattering partners, i.e. the other superparticles.

Having established the scattering rate above, the notation for interacting electrons will be used for simplicity. Using the maximum value for eq.(2.33), or eq.(2.34),$|k_0-k|=\beta$, yields the maximum probability of two electrons interacting

$$\Gamma_{e-e}^{max} = \frac{nme^4}{8\pi\epsilon^2\hbar^3}\frac{1}{N_e}\frac{1}{2\beta} \tag{2.35}$$

This will be used below to test for scattering. Note that this maximum probability will be the same for *all* pairs and is calculated only once. The question is when to test for scattering. The minimum time between two interactions in the total ensemble, is required. Multiplying $\Gamma_{e-e}^{max}$ with the highest possible number of electron interactions the total ensemble maximum rate is obtained as

$$\Gamma_{e-e,N}^{max} = N_e(N_e-1)\frac{\Gamma_{e-e}^{max}}{2} \tag{2.36}$$

where the subscript $N$ denotes the whole ensemble and the factor $1/2$ is to avoid double counting. Now, the time between two successive electron-electron interactions anywhere in the ensemble is obtained by setting

$$t_e = -\ln(r/\Gamma_{e-e,N}^{max}) \tag{2.37}$$

which indicates the maximum size of the time steps if this approach is to be valid. The derivation is equivalent to the derivation of the flight time, see appendix B. At the end of the time $t_e$, i.e. when sufficient time steps have elapsed, random pairs of electrons are selected, $(i,j)$. For each new pair, the inequality

$$r\Gamma_{e-e}^{max} < \Gamma_{e-e}(k_{0,i},k_j) \tag{2.38}$$

is tested. This determines which pair, if any, is scattered at the end of $t_e$ by selecting the first pair to fulfill the above inequality. Pairs are tested in random order, with $i<j$, so that statistical errors are avoided. The detailed code for electron-electron interactions is shown in appendix A. Once a pair is chosen, no more pairs are tested until sufficient time steps have again passed.

With a pair selected the wavevectors, $k_{0,i}$ and $k_j$, are updated according to the scattering angle of the relative momentum vector[7]

$$\theta = \arccos\left(\frac{1-2r}{1+(1-r)\frac{Q^2}{\beta^2}}\right)$$

and a random azimuthal angle, $\phi$. Here $Q$ is the conserved relative momentum given in eq. (2.26). The determination of the direction of the final relative momentum vector, $\mathbf{Q}'$, is described in detail in appendix D. Once this is found the scattered carriers are updated according to[10]

$$\begin{aligned} \mathbf{k}'_{0,i} &= \mathbf{k}_{0,i} - \frac{1}{2}(\mathbf{Q}' - \mathbf{Q}) \\ \mathbf{k}'_{j} &= \mathbf{k}_{j} + \frac{1}{2}(\mathbf{Q}' - \mathbf{Q}) \end{aligned} \tag{2.39}$$

Since this procedure is limited to maximum one carrier-carrier scattering of each kind, each simulation step, it assumes that the time steps are sufficiently short.

The long-range part, or carrier-plasmon scattering, was implemented into the program in a similar way as the other rates[1] and no detailed description is necessary.

## 2.4 Pauli principle

The Pauli principle was implemented into the program. The theory and procedure described below is based on the work of Lugli and Ferry[13].

### 2.4.1 Theory of the Pauli principle

The Pauli principle says that only one fermion may occupy any quantum mechanical state. This will affect dense areas of the reciprocal space such as the bottom of the Γ-valley since the electrons cannot all occupy the $k = 0$-state. This forces some electrons to have higher energies.

To see how this works periodic boundary conditions are assumed. If the volume is given as a box, $V = L^3$, then the restrictions on k are

$$\begin{aligned} k_x &= \frac{2\pi n_x}{L} \\ k_y &= \frac{2\pi n_y}{L} \\ k_z &= \frac{2\pi n_z}{L} \end{aligned} \tag{2.40}$$

where $n_x$,$n_y$,$n_z$ are integers. The number of states available in a volume $\Omega$ in reciprocal space, or k-space, will then be[5], also counting spin states,

$$\frac{2\Omega V}{8\pi^3} \tag{2.41}$$

### 2.4.2 Implementation of the Pauli principle

In eq. (2.5) some approximations are made. The actual scattering probability must of course include an occupied initial state and an available final state so that

$$P(k, k') = \Gamma(k, k') f(k)[1 - f(k')] \tag{2.42}$$

where $f(k)$ is the probability that the state is occupied. Usually in Monte Carlo simulations one assumes $f(k) = 1$ and $f(k') = 0$. The former can of course be considered true, but when the Pauli principle is taken into consideration the latter can not. The problem becomes to consider the normalized probability function, $f(k)$, for each scattering. Lugli and Ferry[13] suggested a procedure that was used and is described below.

In order to obtain the distribution function k-space must be divided into some volume elements, $\Omega$, and the number of electrons in each counted. The obvious way is to say $\Omega = \mathrm{d}V = \mathrm{d}k_x\mathrm{d}k_y\mathrm{d}k_z$ and create a three dimensional grid of k-space. For simulation purposes it is much more efficient to simplify to the isotropic case so that $\Omega = \mathrm{d}V = 4\pi k^2\mathrm{d}k$. This poses no limitations on the program as long as the bands used are isotropic (see eq. (2.51)) and no external field is applied. A one dimensional grid representing spherical shells in k-space can then be constructed so that the number carriers in each can be counted. The maximum number of allowed particles in each volume element, $\Omega$, is used for normalization and is shown in figure 2.2.

Using eq. (2.41) the volume factor, $V$, must be replaced in bulk simulations. This can be done by modifying the equation to give the number of states available for superparticles by using eq. (2.17)

$$\frac{1}{N_{ratio}}\frac{2\Omega V}{8\pi^3} \tag{2.43}$$

Using eq.(2.17), eq.(2.43) can now be rewritten to[13]

$$N_c = \frac{N_{sup}}{n_e}\frac{2\Omega}{8\pi^3} \tag{2.44}$$

which gives the number of available states that normalizes the distribution function so that

$$f(k) = \frac{N_{cell}}{N_c} \tag{2.45}$$

where $N_{cell}$ is the number of superparticles in the cell determined by $k$. This occupancy must be recorded throughout the simulation.

Returning to the problem of the scattering probability it can be tested whether the final state was available by checking the inequality

$$f(k) < r \tag{2.46}$$

where $r \in [0, 1]$. If it is fulfilled the particle is scattered and it's momentum updated. The final state was then considered available. If not, it is treated as self scattering.

## 2.5 CMT valence band structure

A new model for the valence bands was implemented so that the simulated bandstructure would resemble that of $Cd_xHg_{1-x}Te$. Simulations of GaAs used the valence band structure given in the project report[1].The model for the light hole band was based on the approach given by Lund[14]. He showed that in narrow band gap semiconductors,

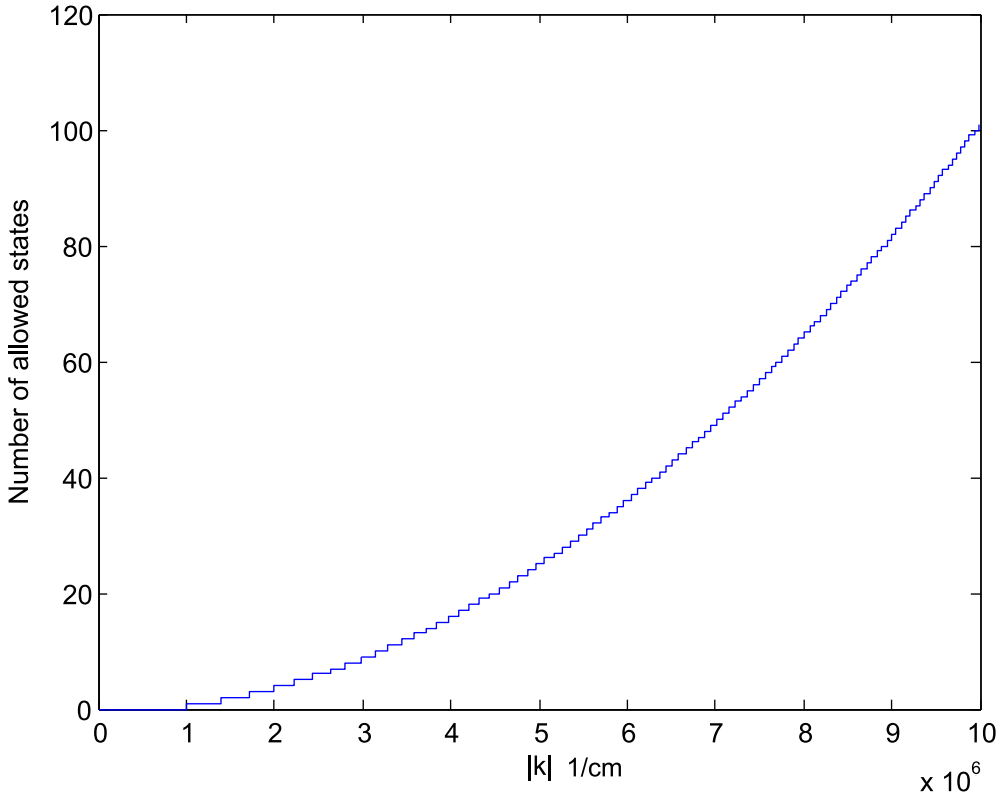


**Figure 2.2:** The number of allowed superparticles, $N_c$, in shell-shaped volume elements given by eq. (2.44). In this case the total number of superparticles was $N_{sup} = 10000$, d$k = 10^4 cm^{-1}$ and $n_{el} = 10^{23} cm^{-3}$.

such as $Cd_xHg_{1-x}Te$, the interaction between the conduction band and the light hole band is the most important. Ignoring the interaction with other bands yields the Kane model[14]

$$E'(E' - E_G)(E' + \Delta_0) - k^2P^2(E' + 2\Delta_0/3) = 0 \tag{2.47}$$

where $E' = E(\mathbf{k}) - \frac{\hbar^2 k^2}{2m_0}$, $\Delta_0$ is the split-off energy and $P$ is the matrix element containing the $\mathbf{k} \cdot \mathbf{p}$ interaction. $E_G$ is the band gap at $k = 0$ described given by eq. (2.50). This is an third order equation whose solutions are the conduction, split-off and light hole bands. In the Monte Carlo program only the light hole band is currently of interest, as the conduction band is modeled as three individual valleys and the split-off band is neglected. The solution for the light hole band is

$$E(\mathbf{k})_{LH} = -2\sqrt{-p}\cos\left(\arccos\left(\frac{-q}{\sqrt{-p^3}}\frac{1}{3}\right) + \frac{\pi}{3}\right) - \frac{b}{3} + \frac{\hbar^2 k^2}{2m_0} \tag{2.48}$$

where

$$\begin{aligned} q &= \frac{b^3}{27} - \frac{bc}{6} + \frac{d}{2} \\ p &= \frac{c}{3} - \frac{b^2}{9} \\ b &= \Delta_0 - E_G \\ c &= -(E_G\Delta_0 + P^2k^2) \\ d &= -2\Delta_0 P^2 \frac{k^2}{3} \end{aligned} \tag{2.49}$$

One important aspect of $Cd_xHg_{1-x}Te$ is that it is an narrow band gap alloy. This was partially compensated for by introducing the following empirical band gap energy for CMT given by Lund[14]

$$E_G = -0.304 + 5 \cdot 10^{-4}T + (1850 - T) \cdot 10^{-3}x \tag{2.50}$$

where $x$ is the alloy fraction and $T$ is the temperature. One further adaption to an alloy is the inclusion of alloy scattering given in eq. (2.6). Other affected material parameters can be found in appendix E.

The interaction with the heavy hole band was neglected in eq. (2.47), therefore it must be handled independently. A semi-analytical model was originally used to model the heavy hole band[15] [1] in GaAs. This was replaced by an empirical model obtained from FFI to represent CMT

$$E(\mathbf{k})_{HH} = \begin{cases} -Ak^2 + Bk^4 - Ck^6, & k \leq k_{zone} \\ -E(k_{max}) + D(k - k_{max})^2 - F(k - k_{max})^4 & k > k_{zone} \end{cases} \tag{2.51}$$

where $A$,$B$,$C$,$D$ and $F$ are empirical coefficients which are given in appendix C. $k_{zone}$ is an empirical value where the splices meet. Note that this band is not warped like the one for GaAs[15] [1], i.e. the direction of $\mathbf{k}$ does not matter.

The valence bands described above form a band structure like the one shown in figure 2.3. Clearly there is something wrong with the light hole band for large $k$. This is clearly due to the addition of the free carrier term, $\frac{\hbar^2k^2}{2m_0}$. Because of this, an *ad. hoc.* fix was introduced to the LH-band for large values of $k$. More precisely, for $k > k_{zone}$ it simply mimics the shape of the heavy hole band as shown in figure 2.4. For comparison purposes the valence band structure of GaAs is also shown in figure 2.5.

### 2.5.1 Finding final k in the valence bands

When determining final states, only the final energy is most often available. A way to determine the length of the final k-vector after scattering is necessary. The direction is determined from scattering angles, $\theta$ and $\phi$, by a separate technique as described in appendix D.

In order to find the length of $\mathbf{k}_f$ either eq. (2.51) or eq. (2.48) must be inverted to $k_f = k(E_f)$. Due to the involved form of these equations this is rather difficult to do

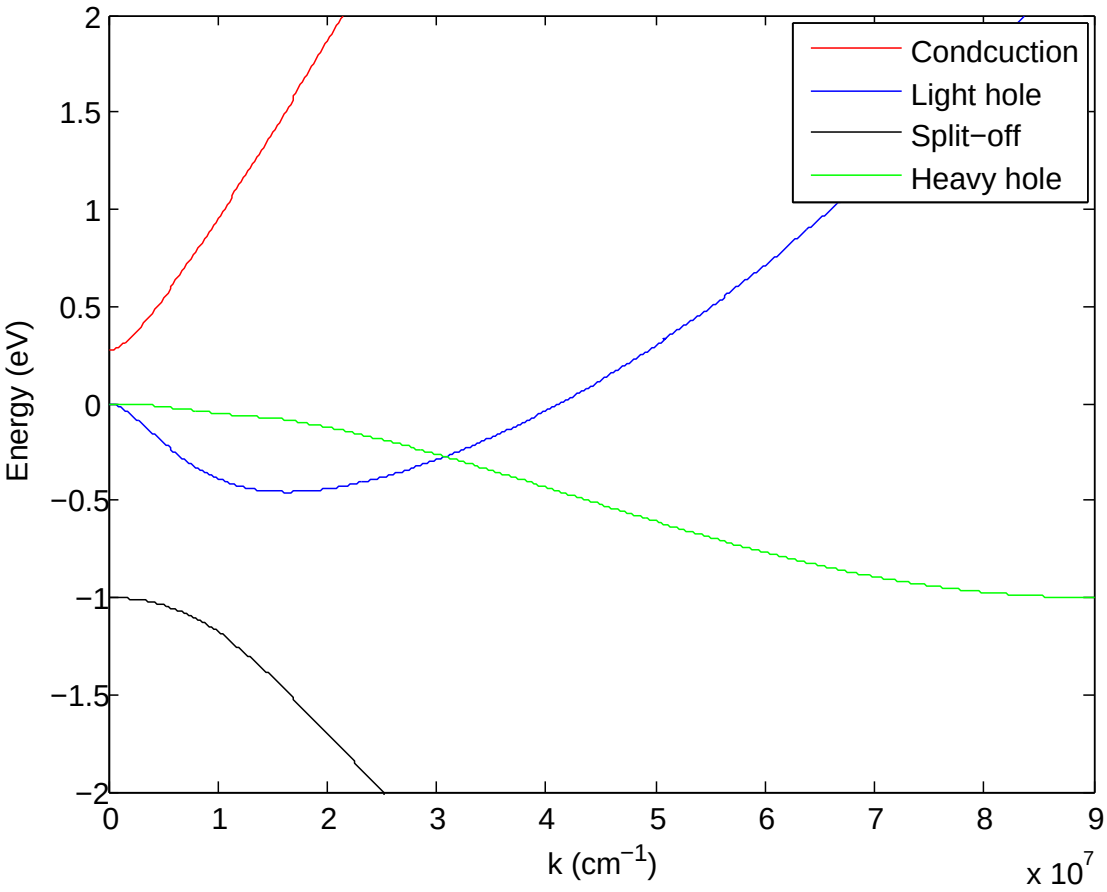


**Figure 2.3:** The band structure obtained from solving eq. (2.47) as well as the heavy hole band from eq. (2.51). The conduction and split-off bands were not included in the program, but are shown for comparison purposes. The behavior of the light hole band away from $k = 0$ is clearly not physical and is due to the addition of the free carrier term, $\frac{\hbar^2 k^2}{2m_0}$, to the light hole band solution.

analytically. In stead, the valence bands and the corresponding length of the momentum vector can be tabulated in the beginning of the simulation. This works very similar to the way the scattering rates were determined in section 2.2.3 including the interpolation in eq. (2.16).

When tabulating the length of the k-vector, the need arises for some maximum value of k. Here the periodicity of the simulated crystal structure is helpful. In reciprocal space the Wigner-Seitz primitive cell, i.e. the smallest periodic structure in the crystal, is called the Brillouin zone[16]. A reciprocal lattice vector can be constructed according to

$$\mathbf{G} = n_1\mathbf{b}_1 + n_2\mathbf{b}_2 + n_3\mathbf{b}_3 \tag{2.52}$$

where $n_i$ are integers and $\mathbf{b}_i$ are the primitive vectors of the reciprocal lattice. The various $\mathbf{G}$ will therefore describe the Brillouin zone. It also has the properties

$$(\mathbf{k} + \mathbf{G})^2 = k^2 \tag{2.53}$$

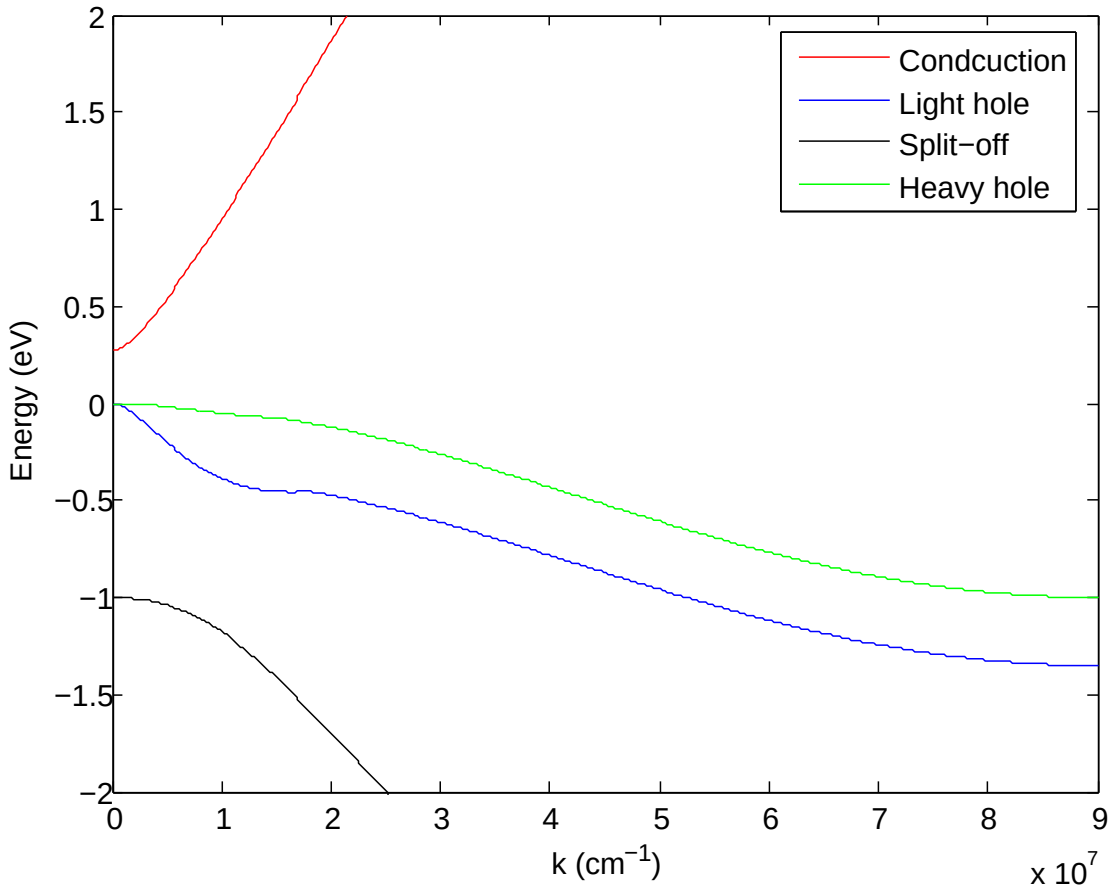


**Figure 2.4:** The band structure obtained from solving eq. (2.47) as well as the heavy hole band from eq. (2.51). The conduction and split-off bands were not included in the program, but are shown for comparison purposes. The fixed light hole band mimics the heavy hole band for large $k$. Though this is a crude approximation it is better than figure 2.3.

and

$$e^{i\mathbf{R}\cdot\mathbf{G}} = 1 \tag{2.54}$$

where $\mathbf{R}$ is the real-space periodicity of the crystal as given in section 2.1.1. This means physically that, due to the periodicity of the crystal, that a $\mathbf{k}$ extending beyond the Brillouin zone can be shifted by some $\mathbf{G}$ so that it is within without loss of any physical properties. This means that the k-vector at the zone boundary is a natural maximum value for the tabulation. In an isotropic fcc lattice, as assumed for both GaAs and CMT, this is

$$k_{max} = \sqrt{3}\frac{\pi}{a} \tag{2.55}$$

where $a$ is the lattice constant. In the simulation, therefore, whenever the momentum vector is grater than $k_{max}$, i.e. $k > \sqrt{3}\frac{\pi}{a}$, it is shifted back into the Brillouin zone via $\mathbf{k}' = \mathbf{k} \pm \mathbf{G}$.

Turning to the analytical approach, it is limited by approximations when inverting the energy equations. In the current work approximations were made for the small $k$ regions

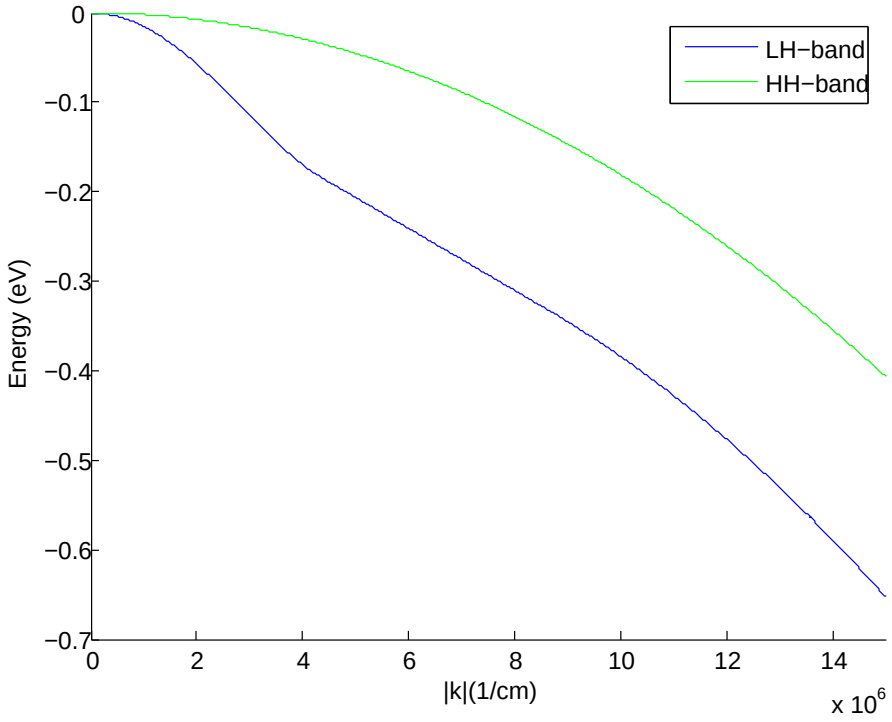


**Figure 2.5:** The valence band structure for GaAs. Details concerning this is given in the project report[1]. It can be seen from comparison that CMT is more non-parabolic than GaAs. Only the central part of the band structure is shown here to illuminate the non-parabolicity. For larger k, the GaAs model is mostly parabolic.

of eq. (2.48) and eq. (2.51). The inner part of the light hole band was curve fitted using Matlab and the same part of the heavy hole band was approximated by neglecting the $k^6$-term. This analytical approach was tested and compared to the tabulation approach given above. The resulting expressions were

$$k_{final,HH} = \begin{cases} \pm\sqrt{\frac{A}{2B}\left(1 + SQRT(1 - \frac{4BE_{final}}{A^2})\right)}, & k < k_{zone} \\ k_{zone} \pm \sqrt{\frac{D}{2F}\left(1 + SQRT(1 - \frac{4F(E_{final}+E_{HH,zone})}{D^2})\right)}, & k > k_{zone} \end{cases} \tag{2.56}$$

$$k_{final,LH} = \begin{cases} \frac{p_2}{2p_1}\left(1 \pm \sqrt{1 - \frac{4(p_3 - E_{final}p_1^2)}{p_2^2}}\right) & k < k_{zone} \\ k_{zone} \pm \sqrt{\frac{D}{2F}\left(1 + SQRT(1 - \frac{4F(E_{final}+E_{LH,zone})}{D^2})\right)}, & k > k_{zone} \end{cases} \tag{2.57}$$

Specific parameters used were obtained from FFI and *The Particle Data Group*[17], some fitting parameters were also obtained using Matlab. It was also necessary to introduce some upper boundary condition in order to determine $D$. Details can be found in appendix C.

# Chapter 3

# Results and Discussion

Simulation results and the effects of recent changes are presented and discussed. Results for CMT were obtained using the new bandstructure and material parameters with an alloy fraction $x = 0.275$. These are listed in more detail in appendix E along with material parameters used for GaAs.

## 3.1 Plasmon scattering

The central quantity that determines the plasmon scattering rates is the plasmon frequency given in eq. (2.28), and thus the carrier density. For the two materials considered the plasmon energies are given as

$$\begin{aligned} \hbar\omega_{p,CMT} &= 2.99\,meV \\ \hbar\omega_{p,GaAs} &= 48.75\,meV \quad \text{or} \quad 15.42\,meV \end{aligned} \tag{3.1}$$

depending on the density. For GaAs this was set to $10^{17}\,cm^{-3}$, figures 3.1 and 3.2, and $10^{16}\,cm^{-3}$, figure 3.3, respectively. The density of CMT is determined from the alloy fraction though[3]

$$n_{CMT} = 10^{ax+b}\,cm^{-3} \approx 7.24 \cdot 10^{15}\,cm^{-3}$$

with the alloy fraction,$x = 0.275$. The CMT rates in figure 3.4 seem to indicate that large carrier energies are required for plasmon interactions. This is due to the high energy cut-off in the Γ-valley and also since electrons in the L-valley are energetic. The emission rates are higher than absorption in CMT, meaning that the energetic electrons would produce plasmons as expected. One can from this conclude that plasmon effects would be most active at high energies. From figure 3.4 the rates can be seen to slightly drop off as the energy increases, which is not the case for GaAs. This could be an effect of the narrow band gap in CMT, but precise rates accounting for this, and the great non-parabolicity, should be implemented before any conclusions are drawn.

The scattering rates for GaAs allows for more interpretation since the density can be more directly controlled in simulations. From the scattering rates it can be seen that the absorption rates gradually move to overlap the emission rates as the density decreases. This means that for high energy electrons, the probability of absorbing a plasmon is

greater when the density is low. This can be understood since low density materials should have fewer plasmons. The slightly lower emission rates in figure 3.3 also results in fewer plasmons at low density.

Both emission and absorption rates seem to encounter a cut-off at "low" energies. This can be qualitatively understood since the carriers would need some minimum mobility in order to adopt gas-like behavior, i.e. plasmons, and that this would also be related to the effective mass. The cut-off of for absorption rates is usually lower than for emission. This means that as the carriers cool below the cut-off energy the net effect is plasmon absorption, leaving a "cold" ensemble with relatively few plasmons as expected. When the density is low the rates are near equal, for example there is no clear difference for $n \sim 10^{12}\, cm^{-3}$. This means that the net number of plasmons will not change much with increased carrier energies and thus affects the carriers little. This implies that plasmon effects should be most apparent in high energy, high density situations, which seems reasonable.

One way to improve the carrier-plasmon scattering rates is by accounting for non-parabolicity effects in the Debye screening length. As shown by Gelmont and Lund[2] this will depend on the distribution function and will therefore need to be recalculated at regular intervals. In addition, the plasmon frequency used here is also based on parabolic bands. A procedure for accounting for the non-parabolicity by introducing an effective optical mass to eq. (2.28) is described by Hasselbeck and Enders[18]. Implementation of these corrections could illuminate finer points of the electron-plasmon interaction in CMT and should therefore be considered.

## 3.2 Pauli principle

The overall effect of the Pauli principle is to push the carriers to larger energies. This shift is shown in figures 3.6 and 3.5. The amount the distribution is shifted depends on the carrier concentration as can be seen for the same figures. This result was expected from the theory described above.

The number of allowed states in k-space, given in eq. (2.44) and figure 2.2, needs some interpretation. If the value $N_{sup}$ is increased there are room for more in each grid point. This is so because in that case each superparticle would represent fewer actual electrons, since their number, or density, is constant. Since each grid point can fit a given number of electrons, this results in each grid point accommodating more superparticles. This fits well with intuition, as $N_{sup}$ has no physical significance. In fact, only the electron density, $n_{el}$, in eq. (2.44) should influence the simulation, which corresponds well with the results.

As described above, the k-space volume elements, $\Omega$, were chosen as spherical shells. This is sufficient when considering isotropic bandstructures with no external field. When an external field is applied the sphere must be shifted according to the displaced distribution function[19]. However, starting from an optical distribution, where most electrons have a certain $\mathbf{k}$, works without shifting the sphere and can be used to simulate the system after a laser pulse. To minimize the computation required, the jurisdiction of the Pauli principle can be limited to where it is most important, such as the bottom of the $\Gamma$-valley.

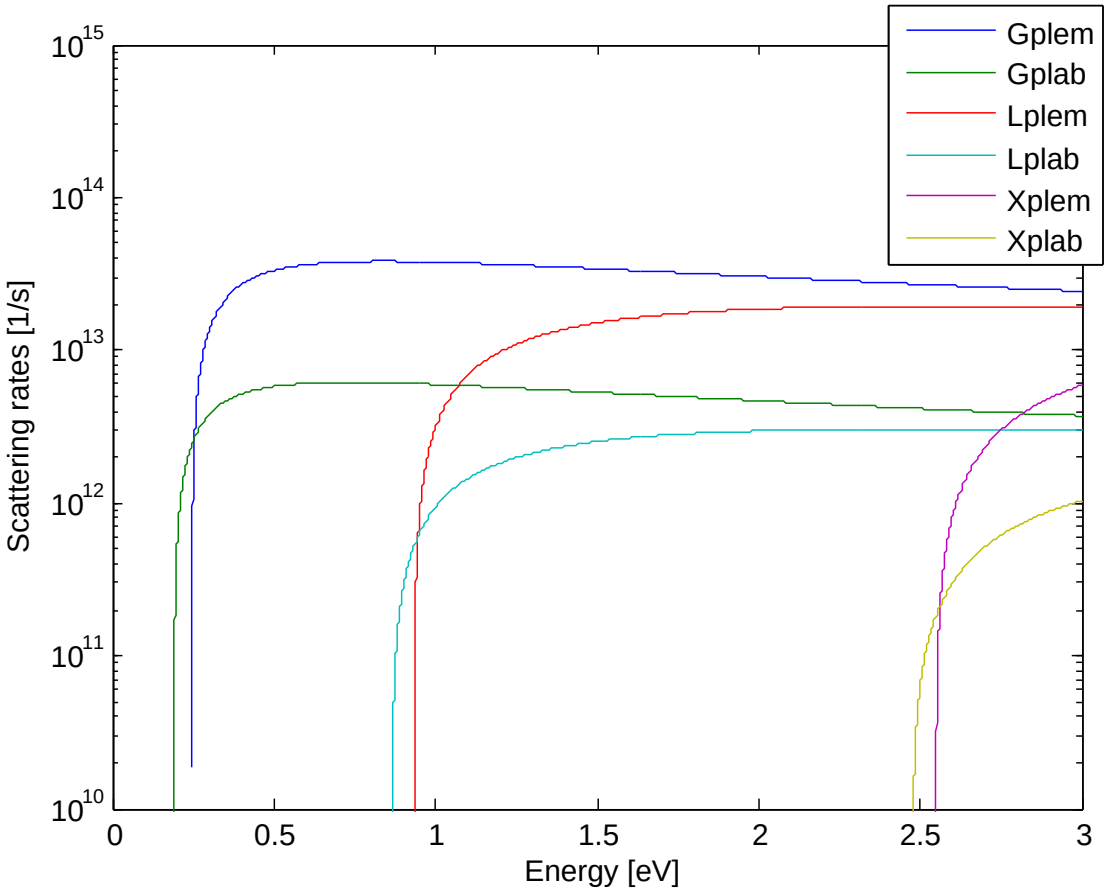


**Figure 3.1:** Electron-plasmon scattering rates in GaAs with carrier density $n = 10^{17}\,cm^{-3}$. The scattering rates are quite high and it can be seen, from the variation between the valleys, that they are very dependent on the effective mass of the electron.

The effect of the Pauli principle is to prevent unphysical concentrations of particles in k-space and it's importance increases with the density. For highly doped materials the bottom of the Γ-valley will be densely packed with electrons. This distribution will be far more realistic with the Pauli principle applied since without it all electrons would drift to the preferable low energy at $k = 0$. It is clear that this feature is important to any semiconductor simulation program so it's inclusion here is justified.

## 3.3 CMT band structure

The band structure of the material affects much of the program, but most of the mechanisms implemented in this report do not directly dependent on it. Because of this the program has been constructed in such a way that the band structure can, with relative ease, be replaced without worrying about the implementation of these mechanisms. Note that a separate version of the program was kept and updated in order to simulate GaAs. In this section, however, results are from the CMT version.

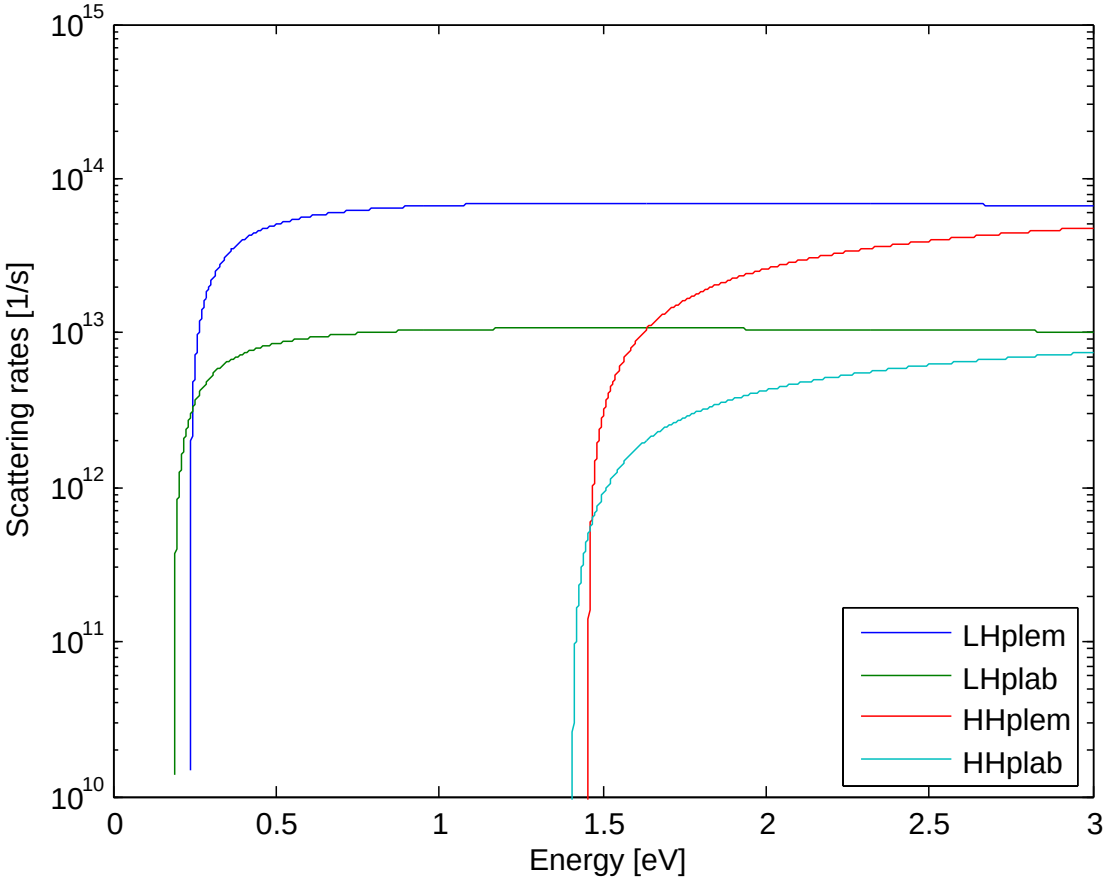


**Figure 3.2:** Hole-plasmon scattering rates in GaAs with carrier density $n = 10^{17}\,cm^{-3}$. The scattering rates are quite high and it can be seen, from the variation between the bands, that they are very dependent on the effective mass.

The most direct result of the band structure lies in the determination of the final momentum vector after scattering, $\mathbf{k}(E_f)$, which results in both the observed energies and the k-space distribution. From a physical standpoint the energy of the system is a good measure for the quality of the program. For instance, one can expect carrier energies around $\frac{<E>}{(3/2)k_BT} \sim 1$ in a steady state solution. An important observation can be made from the energy of the holes in figure 3.7. It is obvious that the entire simulation time is spent approaching some steady state solution, meaning that the initial guess of the k-space distribution is not consistent with the result. In principle, the initial guess is not important since the system will eventually adopt the one emerging from the simulated mechanics. In the Monte Carlo program two options exist for the initial distribution, optical or Gaussian, neither of which corresponds with the simulation. See the example in figure 3.8. The final distribution of the holes is suspicious, and it is the authors opinion that the valence band mechanics can be improved by introducing the Pauli principle here as well. This notion was not indulged due to time limitations, but it will limit the build-up of holes near $k = 0$, providing the program with more realistic hole distributions.

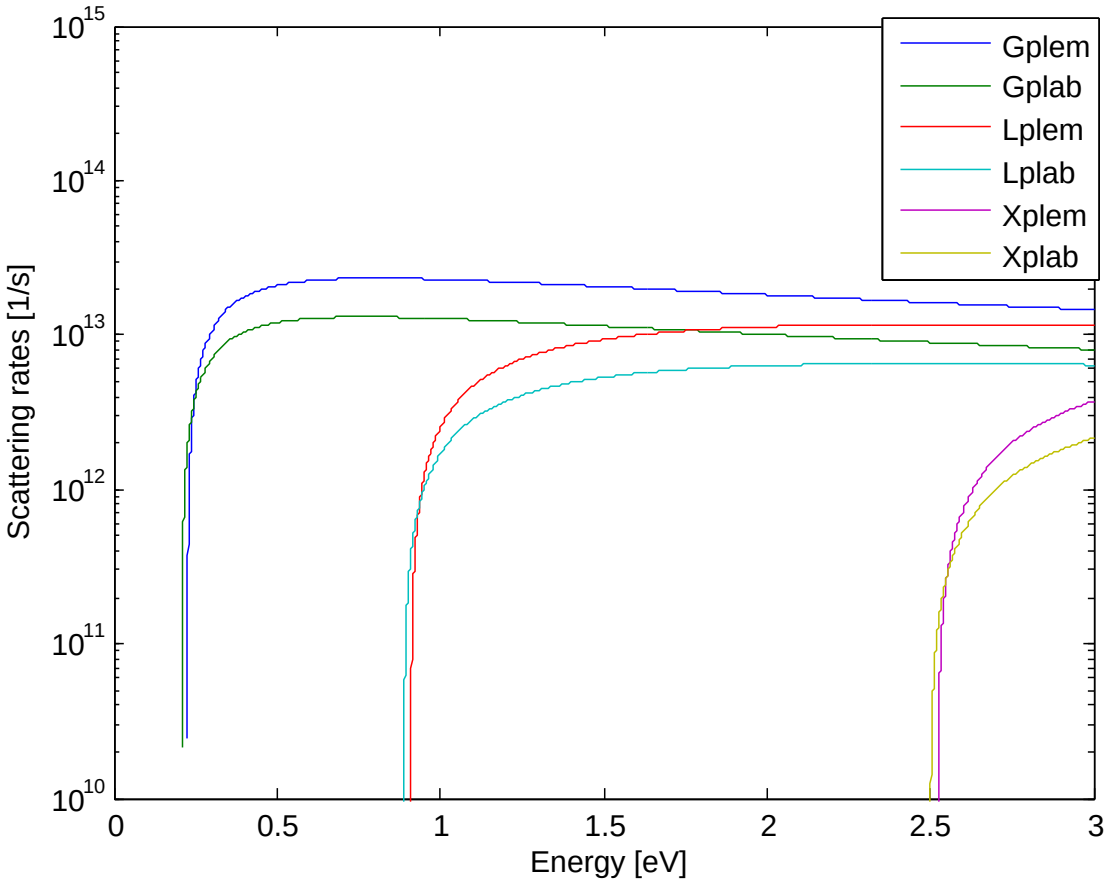


**Figure 3.3:** Electron-plasmon scattering rates in GaAs with carrier density $n = 10^{16}\,cm^{-3}$. When compared to figure 3.1 the dependence on carrier density is evident. At this low density the difference between the absorption and emission rates disappear for low energies.

The work on the final k-vector illuminated some shortcomings in the program. In addition to some minor restructuring of the flight-time routine, the calculation of the direction of the final k-vector was found to be erroneous. This calculation had to be re-derived by the author to ensure that the length of the final k-vector was conserved in the rotation. This is described in detail in appendix D.

The newly introduced CMT band structure is isotropic, unlike the one for GaAs[15]. This is due to its empirical nature since CMT is a less investigated alloy than GaAs. In the immediate future, however, this will be replaced by an 8x8 $\mathbf{k} \cdot \mathbf{p}$ band structure currently being developed at FFI. For details about this method see the project report[1]. As well as being more theoretically accurate this will introduce warping, or directional dependence, of the bands and is bound to improve the program.

Some consideration of the method for finding the length of the final k-vector is in order. In the end, the tabulation of the valence band energies produced results that best fitted expectations and was therefore chosen as the main approach. All results presented here were obtained using tabulation. Either method, however, has its benefits and drawbacks. As mentioned in section 2.5.1, the calculation of the final momentum vector has a large

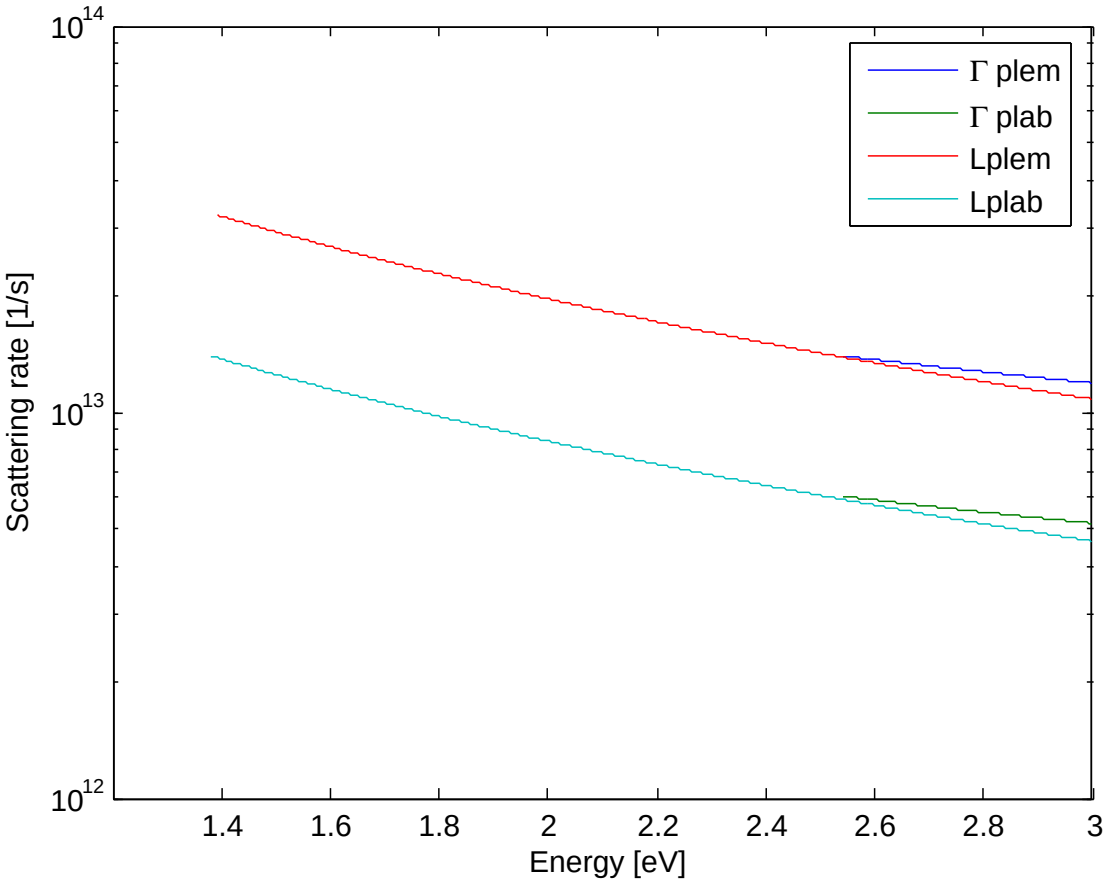


**Figure 3.4:** The plasmon scattering rates in CMT using $x = 0.275$. The rates in the X-valley and hole bands appear as zero in this simulation. The rate in the L-valley appears only at high energies, and the Γ-valley even higher. The scattering rates are extremely dependent on material parameters such as density and alloy fraction.

effect on the energy in the simulation and is therefore very important.

### 3.3.1 Final k via analytical approach

This method was, in the end, not used to generate results since it proved less accurate than the tabulation method, but is included for completeness. Calculating the final k from analytical expressions is, in principle, more precise than using look-up tables, but owning to the involved form of the dispersion relation approximations were made. With these approximations the analytical approach proved less reliable in producing accurate results. For large k, an analytical approach has no obvious limit. However, with the Brillouin zone introduced as described in eq. (2.55), the average energy was reduced from $\frac{<E>}{(3/2)k_BT} \sim -30$ to $\frac{<E>}{(3/2)k_BT} \sim -10$. This shows the importance of introducing this periodicity. The holes were still very energetic, or "warm", considering that this relation is expected to be $\sim -1$ for steady state.

The initial, Gaussian distribution of the holes in k-space was not preserved and resulted

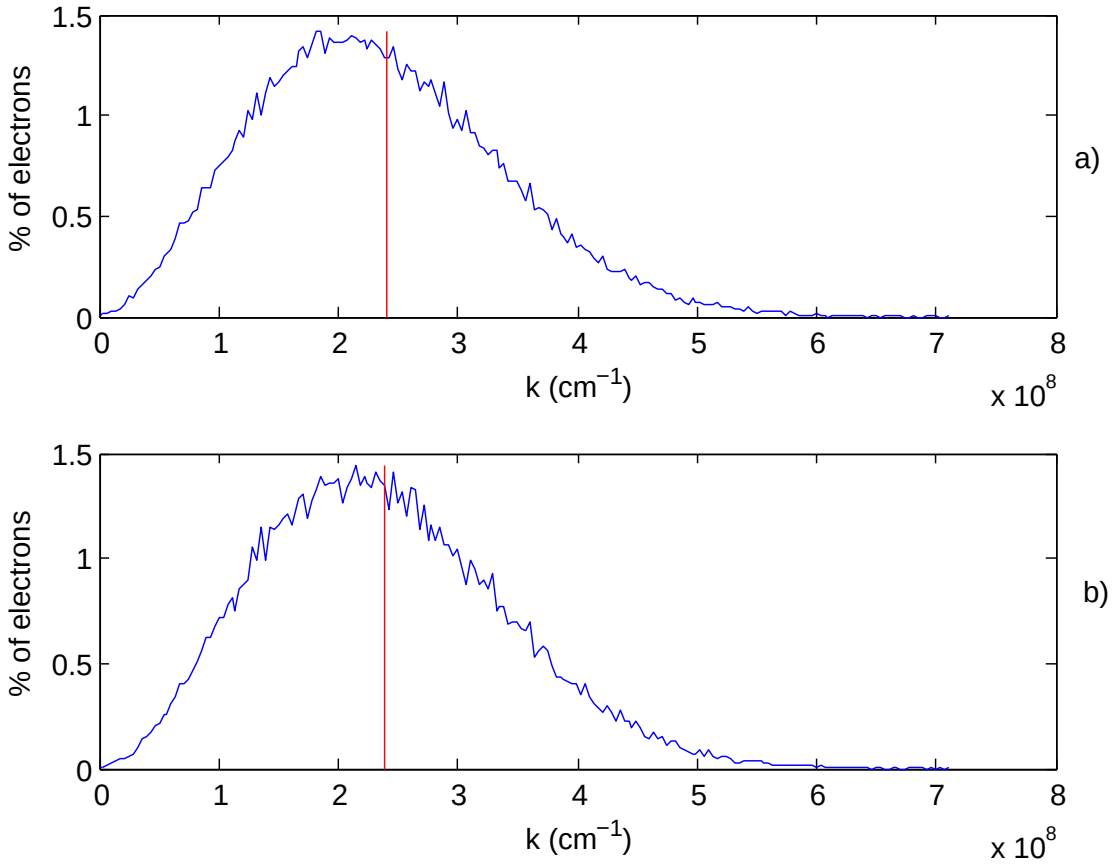


**Figure 3.5:** Initial k-space distribution of electrons with density set to $10^{12}\,cm^{-3}$. *a*) shows the distribution when it is subjected to the restrictions of the Pauli principle and *b*) is when it is not. The shift in energy is not clear at all. Calculations showed that the average $|k|$ in *a*) is only 0.13% larger than in *b*), this is represented by the red lines.

in clustering near $k_{zone}$ and near the band edge. In fact, most holes ended up in either of these locations and the latter partially explains the high energy. However, results showed that the holes relaxed as expected after being exposed to an external field meaning that cooling mechanisms worked despite the relative high energy of the holes. This high energy and the unphysical distribution led to the tabulation approach being superior.

### 3.3.2 Final k via tabulation approach

This approach improved the hole energies so that $\frac{<E>}{(3/2)k_BT} \sim -1.15$ as shown in figure 3.7. Though this is not a perfect result, it is better than the analytical one. Also, since this result is nearly correct it illuminates more subtle results such that the holes relax back to this steady state when an external field is switched off as shown in figure 3.10. This cooling effect is dependent on the relation of the phonon absorption and emission rates since these are the mechanisms of energy exchange with the lattice. These scattering mechanisms depend on material parameters used that may not be entirely precise due to their scarcity for CMT. More importantly, the rates assume a parabolic band structure,

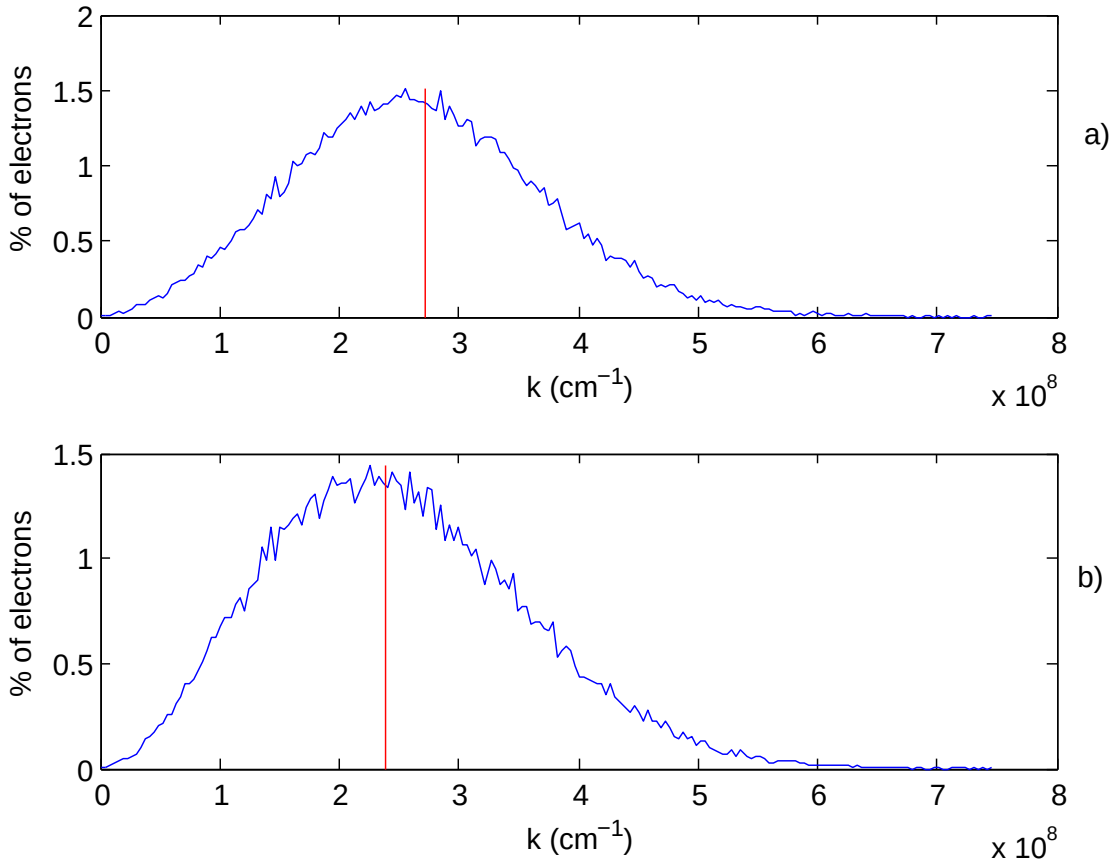


**Figure 3.6:** Initial k-space distribution of electrons with density set to $10^{18}\,cm^{-3}$. *a*) shows the distribution when it is subjected to the restrictions of the Pauli principle and *b*) is when it is not. A clear shift in the distribution can be seen. In this case the average $|k|$ in *a*) is 13.5% larger than in *b*), both are shown with a red line. It is clear that the carrier density is significant.

which is not the case in the program. Thus, the cooling mechanisms could possibly be improved by the procedure described in the project report [1] for non-parabolic scattering rates.

The final distribution of holes in k-space do not match the initial guessed Gaussian distribution in figure 3.8. Though this may not be unphysical and can be partially be explained by lack of the Pauli principle, it could also point to a potential error in the approach, since tabulating valence bands have acquired a reputation for inducing artificial heating/cooling in the holes. The energy-momentum vector mesh was chosen in a linear fashion. This means that where $\frac{\delta E}{\delta k}$ is low there are few possible energies compared to the number of k-vectors available. The net effect is that holes tend to artificially avoid such regions, where one can normally expect the density of states to be higher. The extent of this effect is of course dependent on how fine the mesh is, which has to be balanced by computation time.

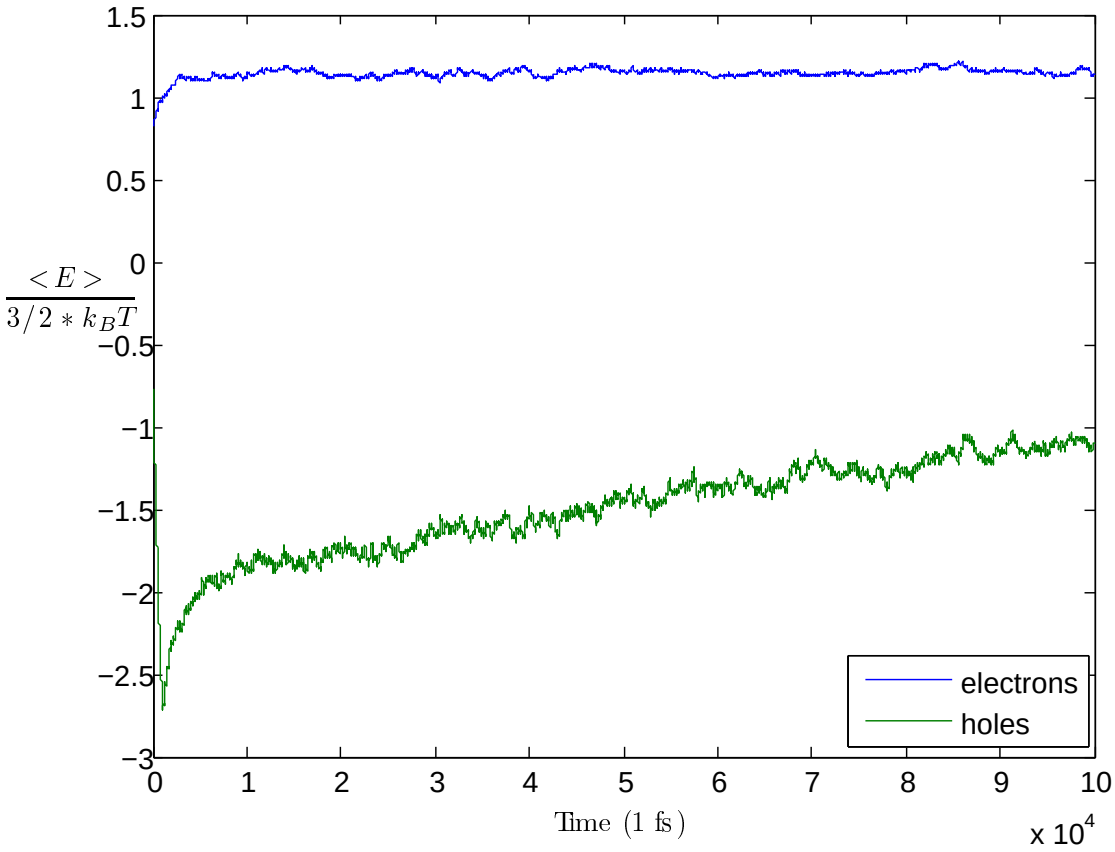


**Figure 3.7:** The average energy of the carriers in CMT compared to the thermal energy. Here 2500 electrons and holes were simulated for 100 ps without any external influence. It can be seen that the system approaches some steady state solution from the initial k-distribution. At the end of the simulation $\frac{<E_e>}{(3/2)k_BT} = 1.16$ and $\frac{<E_h>}{(3/2)k_BT} = -1.15$ which is approximately what is expected. Tabulated values for $k(E_f)$ were used to obtain the hole energies. The density in the simulation was set to $7.24 \cdot 10^{15}\, cm^{-3}$.

## 3.4 Carrier-carrier interaction

This section deals with the short range carrier-carrier interaction given as the second term in eq. (2.19). The interactions caused k-space distributions of carriers to smoothen as expected, since the carriers exchange momentum, but this result will not be emphasized further here. For completeness the maximum scattering rate for two superelectrons is shown in figure 3.9. It may seem curious that this decreases with increased number of superelectrons, but again this is because of the difference between real electrons and superparticles. When the number of superelectrons, increase, each of them represents fewer real electrons. This results in fewer electrons available for interaction and reduces the probability of interaction for the individual superelectron.

It would be far more efficient to the calculations if the scattering mechanism for short-range interactions could be implemented simply as a function of energy, $\Gamma(E)$. Unfortunately it depends on the **k**-vector and, more importantly, on another carrier. This

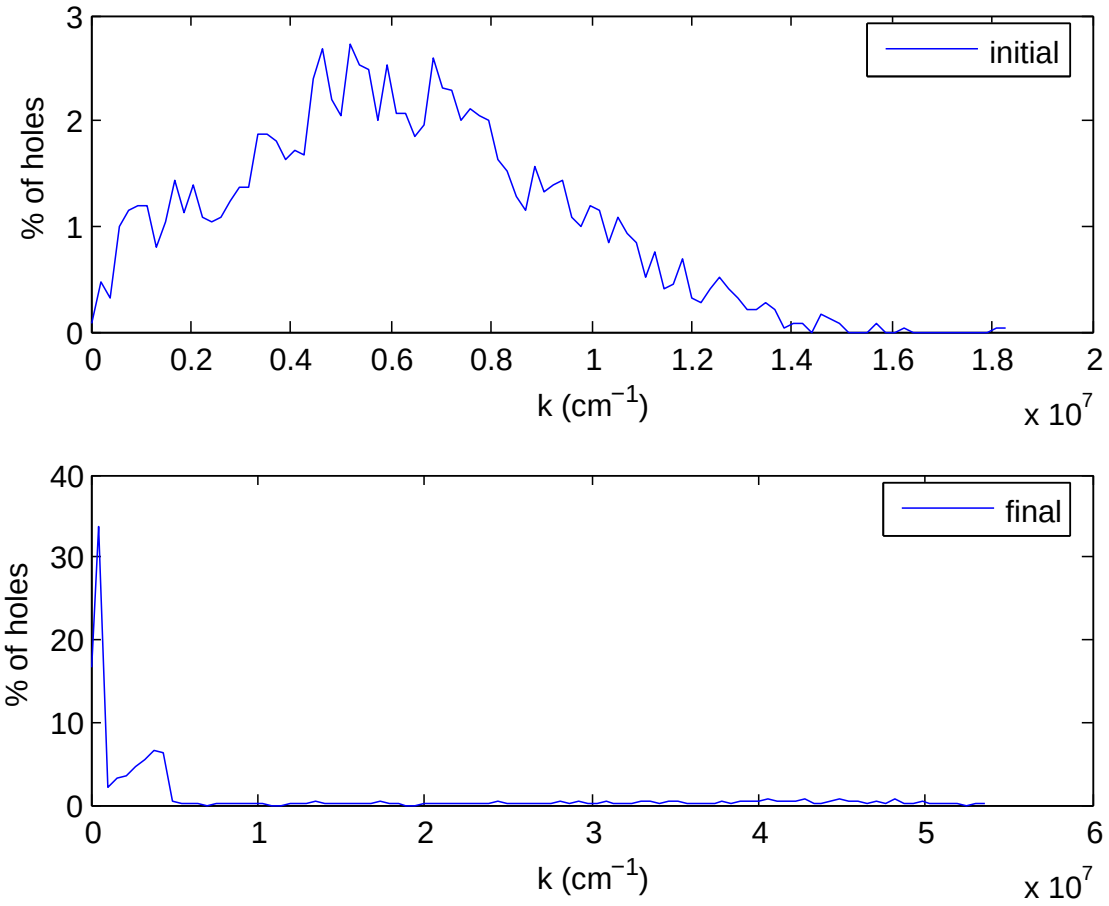


**Figure 3.8:** The initial and final distribution of holes in k-space from the same simulation as in figure 3.7. The holes can be seen as drifting towards $k = 0$ in the final distribution with what is presumably a peak remaining from the initial Gaussian distribution.

can be dealt with in two ways. The first one is to ignore the scattering partner when assessing the final state so that the process is almost a $\Gamma(E)$-type scattering. The problem becomes momentum and energy conservation as only one **k**-vector is updated. The second approach is to simply choose a random partner for the carrier and update their momentum accordingly. The problem with this approach becomes conservation of probability. An electrons scatters according to the rate *and* when it is chosen as a partner. This latter approach was chosen by Ferry and Osman[10]. Mosko[9] concluded that this could be improved by introducing an additional factor 1/2 to the scattering rate and thus account for the "partner" contribution to scatterings. It should be noted that a simplified model based on this approach was investigated in the early days of the Monte Carlo program.

The method used here as given by Mosko[9] avoids the problems above by removing the difference between the scattering carrier and it's partner. Two meticulously chosen electrons are scattered when such a scattering is due, in stead of investigating each electron to see if it is time to scatter. The downside to this approach is that it can require up to $N^2$ calculations (one for each pair) each timestep compared to $N$ calculations (one

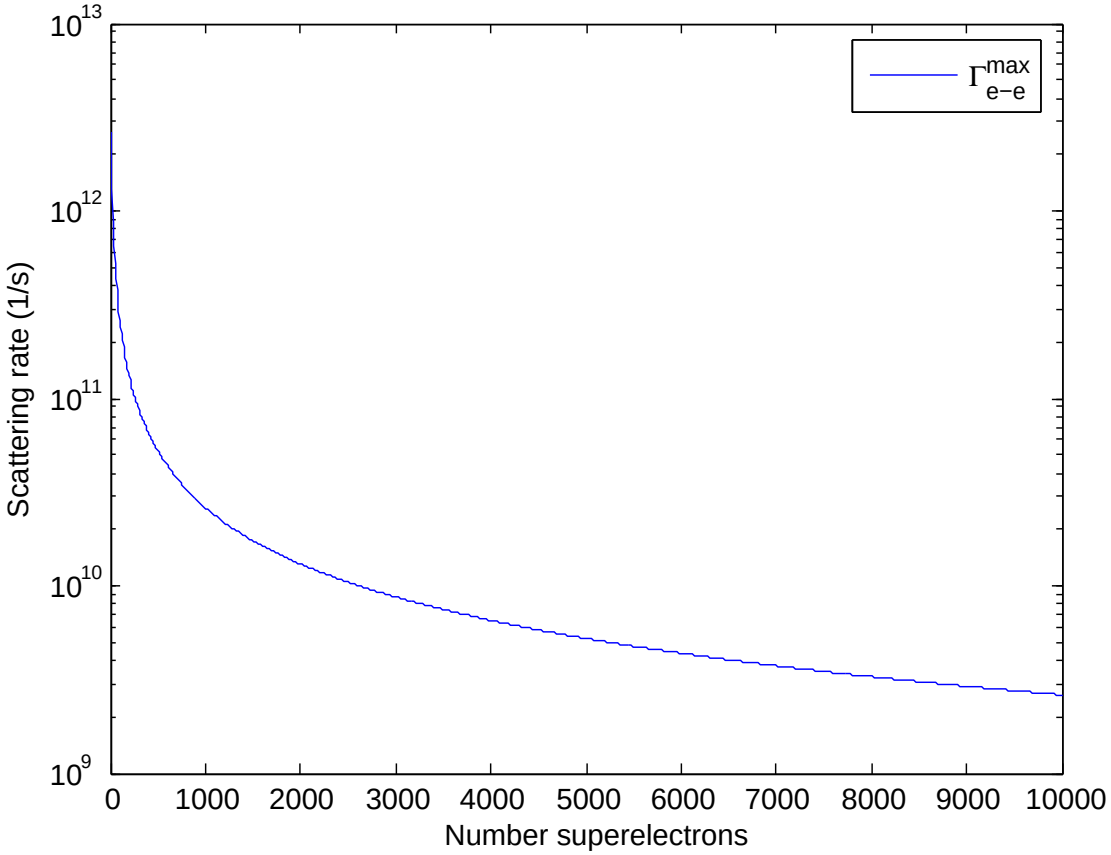


**Figure 3.9:** The maximum scattering probability of a pair of superelectrons as a function of the number of superelectrons. Here the density is $n = 10^{17}\,cm^{-3}$. The maximum rate is also given in eq. (2.35). The decrease is explained in the text.

for each carrier) in the above approaches. Thus one must emphasize either precision or efficiency, which is the common predicament in computational physics. The approach from Mosko uses most of the concepts of Ferry and Osman. This makes it easier to switch to Ferry's approach, should the need arise, than the reverse. This, and the level of precision, was the reason for the chosen approach. It should be noted that it is beneficial to do some testing with simpler models before implementing a more advanced ones as described here.

An other effect of the electron-electron interaction is to cause small fluctuations of the average energy. Mosko[9] showed that if his method is not applied, i.e. the partner electron is unchanged, the average energy either diminishes or increases unphysically, depending on which phonon processes are involved. Here only small fluctuations are seen.

The overall effect of carrier-carrier interactions were small in conventional simulations. In particular, the average energies of the system, such as in figure 3.7, display no distinct changes with the addition of these effects. However, the effect of the interactions still seem to be a slight warming of both electrons and holes. This is better seen in figure 3.10 where the timestep has been made sufficiently short so that the model for carrier-carrier

interactions described in section 2.3 is valid. From the same figure it can also be seen that the electrons initial cooling rate is grater with the carrier-carrier interactions active. This is despite being warmer in steady state at the end. This effect was described by Ferry and Osman[10]. The holes interact more with the lattice than the electrons are therefore cooler. One can from this expect a faster relaxation of the electrons back to steady state when carrier-carrier interactions are active since the electrons can transfer heat to the lattice indirectly, through interactions with holes. This is again confirmed in figure 3.10 since the holes cool slower when they interact with electrons.

Energy transfer from electrons to heavy holes is relatively low due to the huge effective mass of these holes. Therefore the best way for electrons to cool of is to interact with the holes in the light hole band. Unfortunately for the warm electrons the number of light holes is usually very low, and this limits the cooling of electrons. It is therefore plausible that if the number of holes in the light hole band was somehow increased, then the electron cooling should be more effective.

From all this it is clear that carrier-carrier interactions have a substantial impact on heat transfer in simulations and are therefore a vital part of any modern semiconductor simulation program.

As mentioned above the small effect of the carrier-carrier interactions in figure 3.7 is because the time steps in the simulation were not sufficiently small. As seen from figure 3.11, the time between interactions decrease with the number of superparticles. This means that simulating one carrier-carrier interaction of each type each simulation step soon becomes insufficient and severely limits the effects of such interactions. To counter this simulations where carrier-carrier effects are to be investigated should not exceed $N \sim 100$ superparticles in order to ensure that sufficiently short time steps are possible. Matulionis[20] confirmed that macroscopic properties such as drift velocity and average energy do not depend on the number of superparticles in the simulation and so these results are still reliable. Still, larger simulations may be required and one should consider simpler interaction models in these cases.

There may, however, still be ways to reduce calculation times and allow for larger simulations. One way of doing this could be to integrate the carrier-carrier interactions with a Poisson solver[3]. This would have the effect of approximating a real-space location for the carriers. One can then limit the interaction with other carriers to a sphere given, perhaps, by the Debye screening length. This would greatly reduce the number of calculations required each step by the carrier-carrier routine. In fact, the number of possible partners for each electron would only depend on their density, not on their total number. This seems very reasonable from a physical point of view, since the number of simulated particles is without physical meaning. The use of a Poisson solver could, however, require more superparticles in order to obtain statistical precision. Since this involves more calculations it may outweigh the benefits of the procedure.

The conserved quantity in the interaction is obtained though the $\delta$-function in eq. (2.21). This is some relative momentum Q, given in eq. (2.26). When the particles are identical this reduces to $|\mathbf{k}_0 - \mathbf{k}|$ as seen in eq. (2.25). Care was of course taken to account for electrons in different valleys having different effective masses. The problem with the derivation of eq. (2.26) is that it is based on the assumption of parabolic bands. It

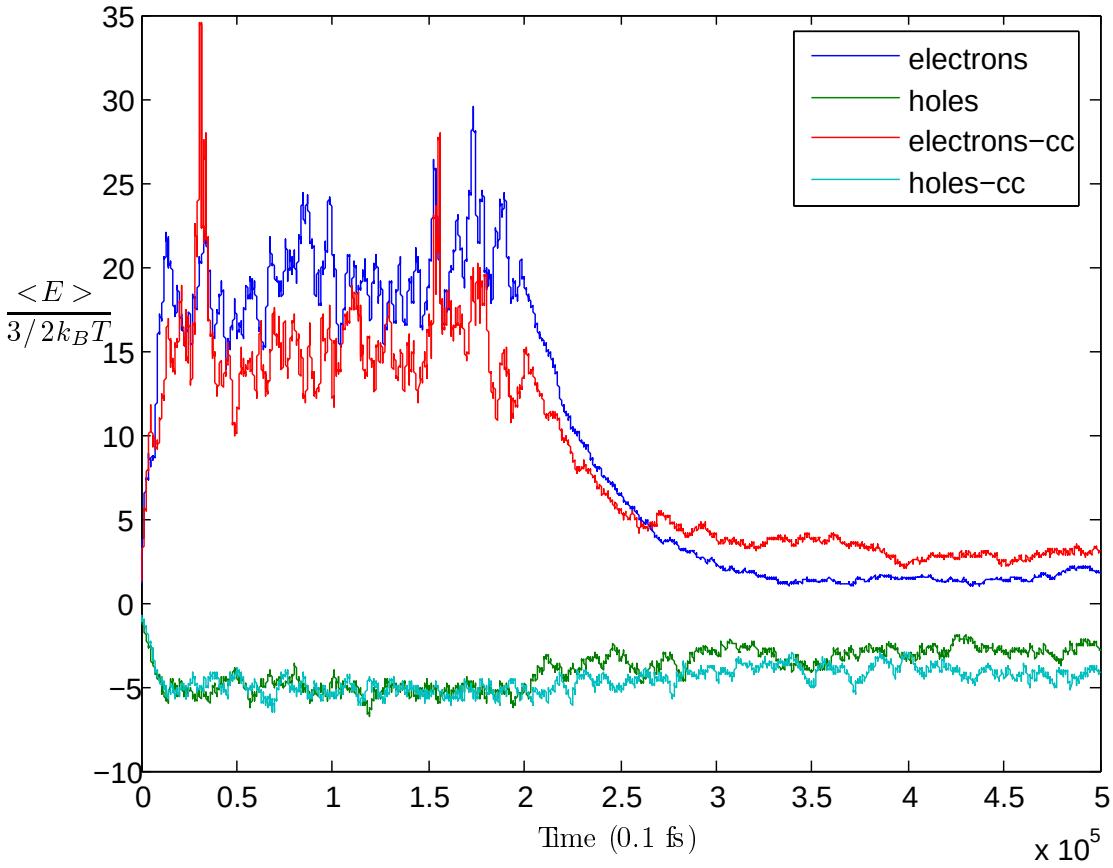


**Figure 3.10:** The average energy of the electrons and holes in CMT here initially under influence of an external field(25 kV/cm). 50 superelectrons and holes were simulated with a timestep of 0.1 fs, with (cc) and without interaction effects. After the system relaxes interacting carriers can be seen to have slightly more energy. Such electrons seem to cool off slightly faster at the expense of the interacting holes. The low number of carriers also resulted in more pronounced statistical fluctuations in average energy.

was beyond the scope of the current work to derive this conserved quantity in the non-parabolic case, but since the band structure in the program is non-parabolic this must be considered a probable source of error. Therefore the rates would greatly benefit from a careful re-derivation which takes non-parabolicity fully into account. In addition it was assumed that $\Gamma_{e-h} = \Gamma_{h-e}$, which is not always valid. Real variation in the carrier densities as well as a difference in the number of simulated carriers would make this assumption false. Because of these approximations some error is to be expected.

An alternative approach to the carrier-carrier interactions is also possible. As mentioned by Jacoboni and Lugli[7], if the flight of the carriers is subdivided into sufficiently small steps it becomes possible to account for the inter particle Coulomb forces by solving classical equations of motion using a total force, $\mathbf{F}(t)$, acting on carriers. These equations for position and velocity can be solved within a finite difference scheme. The total force, $\mathbf{F}(t)$, on a carrier is the sum of inter particle Coulomb interaction and the applied electric field. This is known as the Molecular Dynamics approach. The limitation comes from

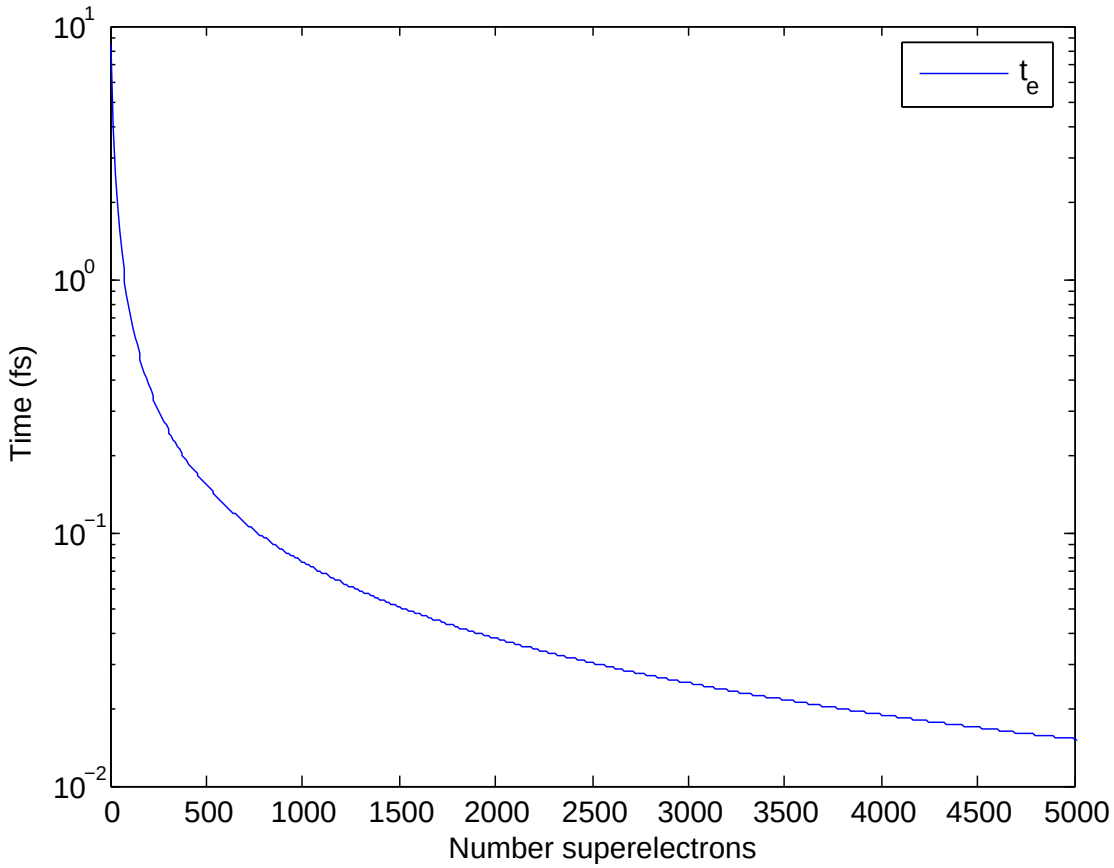


**Figure 3.11:** The minimum time between two electron-electron scatterings when considering the entire ensemble and using maximum scattering rates. This is eq. (2.37) only with $r = 1$. As seen, this decreases with an increased number of superparticles. This limits the number of superparticles the carrier-carrier procedure can successfully simulate. In this case the density was set to $n = 10^{17}\, cm^{-3}$.

the calculation of the inter particle forces, which requires the relative distance between each pair, so again $N^2$ calculations are required. Still, this must be considered a valid contestant to the procedure implemented in this report.

## 3.5 Tabulated scattering rates

The calculation of the various scattering rates were changed so that they were stored in tables at the beginning of the simulation as described in section 2.2.3. Results showed that this approach did not change the precision of the calculations to any noticeable degree and the approximation inherent in the tabulation is therefore considered valid. The overall effect of this approach was to drastically reduce simulation times, which was expected and indeed intended.

Since the individual scattering rates themselves were not altered by this procedure they will not be considered further, and the reader directed to the project report for details[1].

Some minor changes were, however, made to the scattering rates due to the change of material parameters. This did not have dramatic implications and are not emphasized further in this report. The alloy scattering mechanism was also introduced. This was not active in most simulations since an accurate rate required knowledge of the alloy potential, see section 2.1.3. This has to be obtained though experimental means and was not available to the author. The scattering rates included in the program were, however, derived based on the parabolic band approximation. But CMT is highly non-parabolic and it is obvious that better scattering rates that include non-parabolicity are needed. As shown by Gelmont and Lund[2], non-parabolicity effects in the overlap integral can, with fair approximation, be ignored and only the effect on the density of states need be considered in the derivation. This should simplify the implementation of such rates.

Another reason to use tabulated rates was that they add diversity to the program since they enable easy import of scattering rates from other programs. Since much work has been done in this field it is reasonable to allow the program to take advantage of the results from other programs and simulations. One source of such rates is a program developed by Halvorsen[21] to calculate scattering rates. Therefore the Monte Carlo program used in this report is currently adapted to import these "Halvorsen scattering rates" if desired.

# Chapter 4

# Conclusions and Further Work

In the work described in this report many new effects were implemented and many changes were made. Mostly this concerned carrier-carrier interactions. The long range part, or the plasmons, were implemented with relative ease and produced expected results, though the large non-parabolicity in CMT was not fully accounted for. The sort-range interaction had a significant effect on heat transfer in simulations, especially the cooling of electrons. The main drawback was the need for very short time steps and/or few simulated particles. Therefore, in simulations not explicitly investigating carrier-carrier effects, the simpler approaches may be more suitable. This is because the loss of precision in the scattering rate is outweighed by the increased efficiency of the program.

CMT was also added as a simulated material by introducing new material parameters as well as a new valence band structure. This implementation worked fine except that it required tabulation of the energy-momentum relations in order to successfully compute the final momentum after scattering processes.

The implementation of the Pauli principle had the expected effect of shifting the electron distributions to slightly higher energies. It is also clear for the k-space distributions obtained that the valence bands would also benefit from the implementation of this effect.

Tabulating the scattering rates at the start of the simulation drastically reduced simulation times and also enabled the Monte Carlo program to import rates. The program is, however, far from finished and much can be improved. For this reason the further work will be listed here for easy reference, with special emphasis on the effects considered in this report.

- Improve carrier-carrier interactions:
  - Take non-parabolic bands into consideration in the derivation.
  - Integrate with Poisson-solver to limit the choice of partner.
  - Implement an alternative, simpler method for conventional MC simulations.
  - Use non-parabolic Debye screening length.
- Improve valence band structure:

  - Implement 8x8 $\mathbf{k} \cdot \mathbf{p}$ approach.
  - Find analytical approach to final k-vector.
  - Implement Pauli principle in valence bands.
- Implement Pauli for applied external fields via a displaced distribution function.
- Include impact ionization and Auger recombination to vary carrier density throughout the simulation.
- Implement coupled mode-carrier scatterings.
- Include non-parabolicity in density of states and scattering rates.
- Use band structure and data directly from ab initio programs.

# References


[1] Øyvind Olsen. *Modelling of Hole Scattering in a Monte Carlo Transport Kernel for Semiconductors.* Norwegian University of Science and Technology, December 2008.

[2] B. Gelmont, B. Lund, K. Kim, G. Jensen, M. Shur, and T. Fjeldly. Monte Carlo simulation of electron transport in mercury cadmium telluride. *Journal of Applied Physics*, 71, 1992.

[3] Ole Chrisitan Norum. *(Monte Carlo Simulation of Semiconductors - Program Structure and Physical Phenomena).* Norwegian University of Science and Technology, 2009.

[4] A. K. Storebo, T.Brudevoll, Ø. Olsen, O. C. Norum, and M.Breivik. Energy relaxation in IR laser exited $Hg_{1-x}Cd_xTe$. *16th International Conference on EDSION*, 2009.

[5] Jasprit Singh. *Electronic and Optoelectronic Properties of Semiconductor Structures.* Cambridge University Press, first paperback edition, 2007.

[6] T. Brudevoll, T.A. Fjeldly, J. Baek, and M.S. Shur. Scattering rates for holes near the valence-band edge in semiconductors. *Journal of Applied Physics*, 67:7373–7382, 1990.

[7] Carlo Jacoboni and Paolo Lugli. *The Monte Carlo Method for Semiconductor Device Simulation.* Springer-Verlag Wien New York, first edition, 1989.

[8] Geir Uri Jensen. *Monte Carlo simulation of III-V semiconductor devices.* PhD thesis, The Norwegian Institute of Technology, June 1989.

[9] Martin Mosko and Antónia Mosková. Ensamble Monte Carlo simulation of electron-electron scattering: Improvements on conventional methods. *Phys. Rev. B*, 44: 10794–10803, 1991.

[10] M. A. Osman and D.K. Ferry. Monte Carlo investigation of the electron-hole-interaction effects on the ultrafast relaxation of hot photoexited carriers in GaAs . *Phys. Rev. B*, 36:6018–6032, 1987.

[11] D. Bohm and D. Pines. A Collective Description of Electron Interactions: III. Coulomb Interactions in a Degenerate Electron Gas. *Phys. Rev.*, 92:609–625, 1953.

[12] C.G. Olson and D.W. Lynch. Longitudal-Optical-Phonon-Plasmon Coupling in GaAs. *Phys. Rev.*, 177:1231–1234, 1969.

[13] P. Lugli and D.K. Ferry. Degeneracy in the Ensamble Monte Carlo Method for High-Field Transport in Semiconductors. *IEEE Transactions on electron devices*, ED-32:2431–2437, 1985.

[14] B. Lund. *Monte Carlo Simulation of Charge Transport in Semiconductors and Semiconductor Devices.* PhD thesis, The Norwegian Institute of Technology, March 1992.

[15] T. Brudevoll. *Monte Carlo Algorithms for Simulation of Hole Transport in Homogeneous Semiconductors.* PhD thesis, The Norwegian Institute of Technology, May 1991.

[16] Charles Kittel. *(Introduction to Solid State Physics).* Wiley, eighth edition, 2005.

[17] W.-M.Yao et al. *(Particle Data Group).* J. Phys. G 33, 1, 2006.

[18] Michael P. Hasselbeck and Peter M. Enders. Electron-electron interactions in the nonparabolic conduction band of narrow-gap semiconductors . *Phys. Rev. B*, 57 (16):9674–9681, 1998.

[19] Mona Zebarjadi, Ceyhun Bulutay, Keivan Esfarjani, and Ali Shakouri. Monte Carlo Simulation of Electron Transport in Degenerate Semiconductors. *Applied Physics Letters*, 90, 2007.

[20] A. Matulionis, R. Raguotis, and R. Katilius. Interparticle collisions and hot-electron velocity fluctuations in GaAs at 80 K. *Physical Review B*, 56(4):2052–2057, 1997.

[21] Einar Halvorsen. Numerical calculation of valence band structure and hole scattering rates in GaAs. 1991.

[22] Geir U. Jensen, Bjørnar Lund, Tor A. Fjeldly, and Michael Shur. Monte Carlo simulation of semiconductor devices. *Computer Physics Communications*, 67:1–61, 1991.

[23] Charles M. Wolfe, Nick Holonyak, and Gregory E. Stillman. *Physical properties of semiconductors.* Prentic-Hall International, 1989.

[24] Karl Hess. *Advanced theory of semiconductor devices.* Prentice-Hall International, 1988.

[25] Sanjay Kumar Banerjee Ben G. Streetman. *Solid state electronic devices.* Pearson Prentice Hall, 6th edition, 2006.

[26] D.S. Kim. *Monte Carlo Modeling of Carrier Dynamics in Photoconductive Terahertz Sources.* PhD thesis, Georgia Institute of Technology, August 2006.

# Appendices

# Appendix A

# Electron-electron scattering code

Below most of the code dealing with electron-electron scattering is included. Since hole-hole and electron-hole interactions function in the same way, this code is not included. For efficiency no pairs are tested more than once. Only variable declarations and some contingency code is omitted. The code is written in fortran 90/95.

```
1  !  If sufficient time has elapsed SINce the last ee-scatter, then scatter again
2  !  Both carriers are randomly selected and tested with rejection in respect to
       their maximum rate.
3     IF((time-tEE)/timeEE > 1 .AND. (simtype == 1 .OR. simtype == 3)) THEN !perform
          e-e-scattering and recalculate timeEE
4  !     max e-e scattering rate:
5        G=(m1*eC**4*edensity)/(4*pi*epss**2*eps0**2*hbar**3*betasqr*esize)/(2*SQRT(
             betasqr))
6        GE=esize*(esize-1)*G/2.
7        r2=ran(idum) !random number for rejection
8        i=INT(ran(idum)*esize)+1 !starts at random carrier
9        istart=i
10       iwrap=.FALSE.
11       DO p=1,esize
12 !        for reduced mass
13          IF(valley(i) == 'G') THEN
14             Mi=mG
15          ELSE IF(valley(i) == 'L') THEN
16             Mi=mL
17          ELSE IF(valley(i) == 'X') THEN
18             Mi=mX
19          END IF
20          j=INT(ran(idum)*esize)+1 !starts at random partner
21          DO pp=1,esize
22             IF(i == j .AND. j < esize)THEN !cannot scatter on self
23                j=j+1
24                CYCLE
25             ELSE IF(i == j) THEN
26                j=1
27                CYCLE
28             END IF
29 !           avoid counting the same pair twice
30             IF( istart<=j .AND. j<i .AND. (iwrap .EQV. .FALSE.) ) THEN !go to
                  next partner
31                IF(j < esize) THEN
32                   j=j+1
33                   CYCLE
34                ELSE
35                   j=1
```

```
36                      CYCLE
37                   END IF
38                ELSE IF(iwrap .AND. istart<=j) THEN
39                   IF(j < esize) THEN
40                      j=j+1
41                      CYCLE
42                   ELSE
43                      j=1
44                      CYCLE
45                   END IF
46                END IF
47 !              calculate reduced mass
48                IF(valley(j)=='G') THEN
49                   Mj=mG
50 !                    alphaj=alphaG
51                ELSE IF(valley(j) == 'L') THEN
52                   Mj=mL
53 !                    alphaj=alphaL
54                ELSE IF(valley(j)=='X')THEN
55                   Mj=mX
56 !                    alphaj=alphaX
57                END IF
58                M=Mi*Mj/(Mi+Mj)
59 !              calculate relative momentum vector
60                Q1x=2*M*(kx(i)/Mi-kx(j)/Mj)
61                Q1y=2*M*(ky(i)/Mi-ky(j)/Mj)
62                Q1z=2*M*(kz(i)/Mi-kz(j)/Mj)
63                Q=SQRT(Q1x**2 + Q1y**2 + Q1z**2)
64                LL=(M*eC**4*edensity)/(4*pi*epss*epss*eps0*eps0*hbar**3*betasqr* &
65                   esize)*Q/(Q*Q+betasqr)
66                IF(r2*G < LL) THEN !accept scattering
67                   r=ran(idum)
68                   theta=ACOS(1-2*r/(1+Q*Q*(1-r)/betasqr))
69                   phi=2*pi*ran(idum)
70 !                 Finding final realtive wavevector
71                   gamma=ATAN(Q1x/Q1y)
72                   alpha=ATAN( (Q1x*SIN(gamma)+Q1y*COS(gamma))/(Q1z) )
73                   Q2x=Q*( SIN(theta)*COS(phi)*COS(gamma)+SIN(theta)*SIN(phi)*SIN(
                        gamma)*&
74                      COS(alpha)+COS(theta)*SIN(gamma)*SIN(alpha) )
75                   Q2y=Q*( -SIN(theta)*COS(phi)*SIN(gamma)+SIN(theta)*SIN(phi)*COS(
                        gamma)*&
76                      COS(alpha)+COS(theta)*COS(gamma)*SIN(alpha) )
77                   Q2z=Q*( -SIN(theta)*SIN(phi)*SIN(alpha)+COS(alpha)*COS(theta) )
78 !                 Update according to k'=k +- 0.5*(Q'-Q)
79                   dkx=-0.5*(Q2x-Q1x)
80                   dky=-0.5*(Q2y-Q1y)
81                   dkz=-0.5*(Q2z-Q1z)
82 !                 updating wave-vectors
83                   kx(i)=kx(i)-dkx
84                   ky(i)=ky(i)-dky
85                   kz(i)=kz(i)-dkz
86                   kx(j)=kx(j)+dkx
87                   ky(j)=ky(j)+dky
88                   kz(j)=kz(j)+dkz
89 !                 update counter
90                   ScCounter(i,28)=ScCounter(i,28)+1
91                   ScCounter(j,28)=ScCounter(j,28)+1
92                   EXIT !accept
93                END IF
94 !              counter wraps around(partner):
95                IF(j < esize) THEN
96                   j=j+1
97                ELSE
98                   j=1
```

```
99                  END IF
100               END DO
101 !             test accept
102               IF(r2*G < LL) THEN
103                  EXIT !i.e. accept scatter
104               END IF
105 !             counters wrap around:
106               IF(i < esize) THEN
107                  i=i+1
108               ELSE
109                  i=1
110                  iwrap=.TRUE.
111               END IF
112            END DO
113 !          RECALCULATE timeHH
114            tHH=time
115 !          max ensamble total hh-rate:
116            timeHH=-LOG(ran(idum))/GE
117         END IF
```

# Appendix B

# Probability of scattering

A more detailed derivation of eq. (2.12) is presented below. If the probability of an event, such as scattering, occurring in some interval $\Delta t$ is $p(t)\Delta t$ then the probability of it not occurring in the same interval is $(1 - p(t)\Delta t)$. The probability that it has not occurred at all at some time $t$ is then

$$\overline{P(t)} = \prod_0^n \overline{p(t)}\Delta t = \prod_0^n [1 - p(t)\Delta t] \tag{B.1}$$

where $t = n\Delta t$. The problem is the time dependence of the probability density, i.e. $p(t_1) \neq p(t_2)$. Using the 'self-scattering' method this can be avoided. Introducing the maximum probability $\Gamma$ as described in eq. (2.10), the time dependence is traded for some loss in computing time at a later stage. Replacing $p(t) \rightarrow \Gamma$ in eq. (B.1) one obtains the probability that electron has not scattered at a time $t$

$$\overline{P(t)} = \prod_0^n [1 - \Gamma\Delta t] = [1 - \Gamma\Delta t]^n \tag{B.2}$$

From calculus it is known that

$$\lim_{n\to\infty} \left[1 - \frac{\lambda}{n}\right]^n = e^{-\lambda}$$

Since the size of the time intervals, $\Delta t$, is arbitrary this can be used to write eq. (B.2) in a more manageable form. Increasing the number of such intervals, $n$, in such a way that $t = n\Delta t$ remains constant, i.e. $\Delta t \rightarrow 0$, yields

$$\overline{P(t)} = \lim_{n\to\infty} \left[1 - \frac{\Gamma t}{n}\right]^n = e^{-\Gamma t} \tag{B.3}$$

since $\Delta t = t/n$. The probability of a scattering occurring for the first time at a time $t$ is then the total probability that it has not occurred up to that time, eq. (B.3), times the probability of it occurring in the interval $dt$, i.e. $\Gamma dt$, so one obtains

$$P(t_f) = \int_0^{t_f} p(t)_{first\,scattering} dt = \int_0^{t_f} \Gamma e^{-\Gamma t} dt = -\left(e^{-\Gamma t_f} - 1\right) \tag{B.4}$$

Now letting $P(t) \to r$, where $r \in [0, 1]$, one can invert the equation to get

$$t_f = -\frac{\ln(r)}{\Gamma} \tag{B.5}$$

where $1 - r = r$ has been used. This result is the same as obtained in eq. (2.12).

# Appendix C

# Valence band parameters

Here is a list of the parameters used in the empirical valence band structure as well as some further details. For easy reference the light energy is

$$E(\mathbf{k})_{LH} = \begin{cases} -2\sqrt{-p}\cos\left(\arccos(\frac{-q}{\sqrt{-p^3}}\frac{1}{3}) + \frac{\pi}{3}\right) - \frac{b}{3} + \frac{\hbar^2 k^2}{2m_0} & k < k_{zone} \\ (E(k_{zone})_{LH} - E(k_{zone})_{HH}) + E(\mathbf{k})_{HH} & k > k_{zone} \end{cases} \tag{C.1}$$

where

$$\begin{aligned} q &= \frac{b^3}{27} - \frac{bc}{6} + \frac{d}{2} \\ p &= \frac{c}{3} - \frac{b^2}{9} \\ b &= \Delta_0 - E_G \\ c &= -(E_G\Delta_0 + P^2k^2) \\ d &= -2\Delta_0 P^2 \frac{k^2}{3} \end{aligned} \tag{C.2}$$

and heavy hole energy is

$$E(\mathbf{k})_{HH} = \begin{cases} -Ak^2 + Bk^4 - Ck^6, & k \leq k_{zone} \\ -E(k_{max}) + D(k - k_{max})^2 - F(k - k_{max})^4 & k > k_{zone} \end{cases} \tag{C.3}$$

$$\begin{aligned} A &= 7.62 \cdot 10^{-16} \quad \text{eVcm}^2 \\ B &= 3.0 \cdot 10^{-30} \quad \text{eVcm}^4 \\ C &= 5.0 \cdot 10^{-45} \quad \text{eVcm}^6 \\ F &= 0.02 \cdot 10^{-30} \quad \text{eVcm}^4 \\ \Delta_0 &= 1.0 \quad \text{eV} \\ p_1 &= 3.027 \cdot 10^{-38} \\ p_2 &= 9.98 \cdot 10^{-29} \\ p_3 &= 8.64 \cdot 10^{-21} \end{aligned} \tag{C.4}$$

The $p$-variables used to determine $k_{final}$ in the light hole band were obtained by using cure fitting in Matlab, due to the complexities of eq. (2.48). The upper boundary conditions that were used stated that, for the heavy holes, at $k_{max} = 9 \cdot 10^7\,\mathrm{cm}^{-1}$ the energy was $E_{max} = -1\,\mathrm{eV}$. The valence band parameters for GaAs can be found in full detail in the project report[1].

# Appendix D

# Coordinate transforms

With the scattering of two particles the length of the relative momentum, $\mathbf{Q}$, vector is conserved, but it's final direction must be determined. The interaction between the particles lead to two scattering angles, $\theta$ and $\phi$. This is completely analog to the situation where the direction of the final momentum vector $\mathbf{k}_f$ must be determined, like for phonon scatterings, except that the length of the final momentum vector must be used. The former notation will be used here to describe the procedure.

The problem is to translate the final momentum vector,$\mathbf{Q}'$, given by $\theta$ and $\phi$, to the coordinate system of the simulation. There is some freedom in describing the relation of $\mathbf{Q}$ and $\mathbf{Q}'$. If, in some coordinate system $\mathbf{Q}$ lies along the z-direction, then from figure D.1

$$\begin{aligned} Q'_x &= Q\sin(\theta)\cos(\phi) \\ Q'_y &= Q\sin(\theta)\sin(\phi) \\ Q'_z &= Q\cos(\theta) \end{aligned} \tag{D.1}$$

where $Q$ is the conserved length of the vector. Now, this needs to be rotated to the coordinate system of the simulation. It is easier to consider rotating $\mathbf{Q}$ so that it lies along the z-axis and afterwards rotating $\mathbf{Q}'$ back. This can be done with rotation matrices and careful choice of angles. The rotation matrices are

$$R_z(\gamma) = \begin{bmatrix} \cos(\gamma) & \sin(\gamma) & 0 \\ -\sin(\gamma) & \cos(\gamma) & 0 \\ 0 & 0 & 1 \end{bmatrix} \tag{D.2}$$

$$R_x(\alpha) = \begin{bmatrix} 1 & 0 & 0 \\ 0 & \cos(\alpha) & \sin(\alpha) \\ 0 & -\sin(\alpha) & \cos(\alpha) \end{bmatrix} \tag{D.3}$$

where the angles,$\alpha$ and $\gamma$, are defined as the counter clockwise rotation about the axis, x and z respectively, when looking towards the origin. Now consider figure D.1. The plan is to rotate $\mathbf{Q}$ so that it is along the z-axis. It can be seen that

$$\gamma = \arctan\left(\frac{Q_x}{Q_y}\right)$$

Using the projection in the zy-plane, $\mathbf{Q}^{zy}$, yields

$$\alpha = \arctan\left(\frac{Q_y^{zy}}{Q_z^{zy}}\right)$$

This means that $R_x(\alpha)R_z(\gamma)\mathbf{Q}$ lies along the z-axis. Using eq.(D.1) the final vector can now be rotated back to the coordinate system of the simulation using

$$\mathbf{Q}_{final} = R_z(-\gamma)R_x(-\alpha)\mathbf{Q}' \tag{D.4}$$

More explicitly, all this gives the expression of a final vector, $\mathbf{Q}'$, when the original $\mathbf{Q}$ is scattered by an angle $\theta$ and $\phi$.

$$\begin{aligned}
\gamma &= -\arctan\left(\frac{Q_x}{Q_y}\right) \\
\alpha &= -\arctan\left(\frac{Q_x\sin(\gamma) + Q_y\cos(\gamma)}{Q_z}\right) \\
Q'_x &= Q\left(\sin(\theta)\cos(\phi)\cos(\gamma) + \sin(\theta)\sin(\phi)\sin(\gamma)\cos(\alpha) + \cos(\theta)\sin(\gamma)\sin(\alpha)\right) \\
Q'_y &= Q\left(-\sin(\theta)\cos(\phi)\sin(\gamma) + \sin(\theta)\sin(\phi)\cos(\gamma)\cos(\alpha) + \cos(\theta)\cos(\gamma)\sin(\alpha)\right) \\
Q'_z &= Q\left(-\sin(\theta)\sin(\phi)\sin(\alpha) + \cos(\alpha)\cos(\theta)\right)
\end{aligned} \tag{D.5}$$

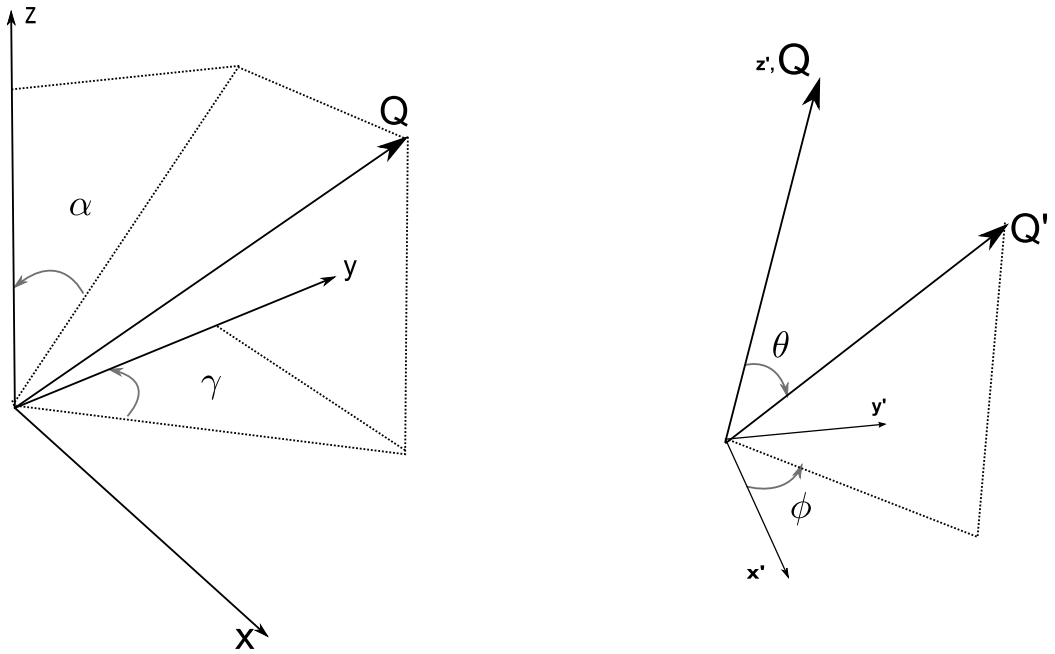


**Figure D.1:** This shows the angles used in the coordinate transform. Note that for the actual rotation back to the simulation system, $-\alpha$ and $-\gamma$ is used. In the right hand figure $Q$ lies along the z-axis of the rotated coordinate system.

The expressions in eq. (D.5) were used in the program to determine the direction of the final momentum vector both for holes and electrons. They were also used to calculate

carrier-carrier scatterings. Note that a common implementation error in using the arctan-functions is that it ignores the signs in the argument. This is, however, easily accounted for.

# Appendix E

# Material parameters

Here the most important material parameters used in the simulations are shown in the tables below. These parameters for CMT were obtained from FFI. Note that for CMT some parameters have fairly complex expressions, such as the energy gap in eq. (2.50), and are not included in the table below.

**Table E.1:** Material parameters for CMT used in the program

| Name | Constant | Value | Unit |
|---|---|---|---|
| Alloy fraction | $x$ | 0.275 | |
| Lattice constant, Hg | $a_{Hg}$ | 6.490 | Å |
| Lattice constant, Cd | $a_{Cd}$ | 6.477 | Å |
| Lattice constant, CMT | $a$ | $xa_{Cd} + (1-x)a_{Hg}$ | Å |
| High frequency dielectric constant | $\varepsilon_\infty$ | 12.25 | |
| Low frequency dielectric constant | $\varepsilon_s$ | $20.5 - 15.6x + 5.7x^2$ | |
| Longitudinal sound velocity | $S$ | 4570 | m/s |
| Split-off energy | $\Delta_S$ | 1 | eV |
| Effective mass in Γ-valley | $m_\Gamma$ | $3\hbar^2 E_g 1.42 \cdot 10^{55}$ | kg |
| Effective mass in L-valley | $m_L$ | $0.222m_0$ | kg |
| Effective mass in X-valley | $m_X$ | $0.580m_0$ | kg |
| Optical phonon frequency | $\omega_0$ | $(8.54x + (1-x)7.18) \cdot 10^{13}/3$ | 1/s |
| Nonparabolicty parameter in Γ valley | $\alpha_\Gamma$ | $(1 - \frac{m_\Gamma}{m_0})^2/E_g$ | 1/eV |
| Nonparabolicty parameter in L valley | $\alpha_L$ | 0.461 | 1/eV |
| Nonparabolicty parameter in X valley | $\alpha_X$ | 0.204 | 1/eV |

**Table E.2:** Material parameters for GaAs

| Name | Constant | Value | Unit |
|---|---|---|---|
| Lattice constant[22] | $a$ | 5.656 | Å |
| High frequency dielectric constant[22] | $\varepsilon_\infty$ | 10.88 | |
| Low frequency dielectric constant[22] | $\varepsilon_s$ | 12.85 | |
| Mass density[22] | $\rho$ | 5317 | kg/m$^3$ |
| Temperature | $T$ | 300 | K |
| Effective mass in Γ valley[23] | $m_\Gamma$ | $0.067 \cdot m_e$ | kg |
| Effective mass in L valley[24] | $m_L$ | $0.222 \cdot m_e$ | kg |
| Effective mass in X valley[24] | $m_X$ | $0.580 \cdot m_e$ | kg |
| Effective mass in HH band[23] | $m_{HH}$ | $0.500 \cdot m_e$ | kg |
| Effective mass in LH band[25] | $m_{LH}$ | $0.074 \cdot m_e$ | kg |
| Optical phonon frequency | $\omega_0$ | 8.55 | 1/s |
| Energy gap[22] | $E_g$ | 1.424 | eV |
| Nonparabolicty parameter in Γ valley[24,26] | $\alpha_\Gamma$ | 0.610 | |
| Nonparabolicty parameter in L valley[24,26] | $\alpha_L$ | 0.461 | |
| Nonparabolicty parameter in X valley[24,26] | $\alpha_X$ | 0.204 | |
| Longitudinal sound velocity[24,26] | $S$ | 5240 | m/s |